Dynamic Mode Decomposition Method -application to the Earth's liquid core

FCTUC FACULDADE DE CIÊNCIAS
E TECNOLOGIA
UNIVERSIDADE DE COIMBRA

João Miguel Rosa Domingos

Department of Physics

University of Coimbra

Under the supervision of

Dr. Maria Alexandra Pais, University of Coimbra

A thesis submitted for the degree of

Master in Physics

September 26, 2014

"Anyone who has never made a mistake has never tried anything new."

- Albert Einstein

Agradecimentos

Este trabalho não teria sido possível realizar sozinho, sem apoio e incentivo. Assim, gostaria de agradecer a todos aqueles que me influenciaram e trouxeram até onde estou hoje.

À Dra. Alexandra Pais, obrigado pelo constante incentivo e apoio ao longo da realização deste trabalho e pela ajuda a fazer com que o próximo passo académico seja possível.

Obrigado a todos os amigos que fiz e levo de Coimbra, fizeram destes anos um aglomerado de experiências e histórias divertidas e felizes que levo comigo para sempre.

Obrigado aos meus pais, Arlindo e Sebastiana, este trabalho é para vocês, pelo apoio incondicional, nos bons e maus momentos, e pelo incentivo para continuar independentemente das dificuldades.

Obrigado ao meu irmão Sérgio, pela inspiração e vontade de ir mais longe.

Obrigado à Magda, que por mais razões do que uma, fez este desafio mais fácil de ultrapassar.

Resumo

Neste trabalho eu aplico o método de decomposição em modos dinâmicos para estudar: primeiro o simples problema de dinâmica de fluidos de um escoamento dentro de uma cavidade; em segundo, o escoamento no núcleo externo líquido da Terra. Primeiro apresento os princípios do método, usado em dinâmica de fluidos para decompor uma sequência complexa e eventualmente perturbada por ruído de cartas de escoamento em componentes onde podemos identificar as mais relevantes em termos da Física do problema. O grupo de dados para estudar o escoamento dentro de uma cavidade é obtido usando o software de livre acesso OpenFOAM. Este caso de estudo é usado como teste para a implementação do meu algoritmo, visto que resultados decorrentes da aplicação do Método da Decomposição Dinâmica podem ser encontrados na literatura. Para os escoamentos no núcleo externo da Terra, dois grupos de escoamentos são usados, obtidos através da inversão de dois modelos de campo geomagnético, GUFM para o período de 1840-1990 e COV-OBS para o período de 1840-2010. Os modos resultantes da decomposição são analisados e comparados a um outro tipo de decomposição do mesmo grupo de dados. Possíveis explicações para os modos principais são apresentadas e discutidas.

Abstract

In this work I apply the dynamic mode decomposition method to study: first the simple fluid dynamic problem of a flow inside a cavity; second, the flow in the liquid outer core of the Earth. I first present the principles of the method, used in fluid dynamics to decompose a complex and eventually noisy sequence of snapshots into components where we can pinpoint those more physically meaningful. The dataset to study the fluid inside a cavity is obtained using the open source software OpenFOAM. This case-study is used as a test for my algorithm implementation, since corresponding results after application of the Dynamic Decomposition Method can be found in literature. As for the flows in the Earth's outer core, two sets of data are used, obtained from inversion of two geomagnetic field models, GUFM for the period 1840-1990 and COV-OBS for the period 1840-2010. The resulting modes of the decomposition are analysed and compared to another kind of decomposition of the same data. Possible explanations for the principal modes are presented and discussed.

Contents

List of Figures

List of Tables

Chapter 1

Introduction

The study of the Earth's magnetic field has been of growing interest in recent years, and many published articles [3], [13], [14] can be found trying to explain its trends, dynamics, variation over time. One practical reason for this growing interest is the study of Space Weather, a field that analyses how the variations of the Earth's magnetic field, directly or indirectly affect our life on Earth. It can influence communications in a world-wide scale, GPS satellites by interfering with guidance and positioning instruments, and can even disrupt electrical networks, by allowing radiation and energetic particles to penetrate the Earth's atmosphere. A very clear example is the South Atlantic Anomaly (SAA), or how it is also known, the bermuda triangle of space. It's an area above the south atlantic region with a very weak magnetic field, and so radiation penetrates much deeper, causing significantly more disruptions in that area, causing a big percentage of satellites malfunctions in orbit.

The consensus over the existence of Earth's magnetic field is that it originates in the convective flow of the Earth's outer core, which is composed of molten metal. The displacement of the electrically conducting fluid relative to the magnetic field lines creates new magnetic field, which will then affect the movement of the liquid, and so on, this theory being known as the geodynamo.

The study of the magnetic field alone can provide us with some answers but to really understand the underlying magnetohydrodynamic (MHD) mechanism, a study of the core flow is the best option. Of course there are no direct ways to retrieve measurements from so far deep in the Earth, approximately from 2900km to 5100km from the surface [13]. The only information we can rely on is the magnetic field produced by the interaction between the flow and the magnetic field through the geodynamo mechanism and measured at the Earth surface or above. It is possible then to invert the data from the magnetic field [16] to allow us to recreate the flow in the outer core, or to be more precise, the flow at the surface of the outer core, next to the so-called core-mantle boundary (CMB). This is not an easy process and requires some restrictions to the allowed flows. In this thesis, I will not be concerned with the geomagnetic field inversion to obtain the Earth core flows. Instead, I will be using flows obtained in other studies considering a quasi-geostrophic (QG) approximation (see section 2.1 and appendix A).

The main goal of the thesis is to create an algorithm to analyse the Earth core flows, based on the method developed by Peter J. Schmid, called Dynamic Mode Decomposition (DMD) [11] [19]. The DMD method analyses data tables of some flow system and separates the different modes that compose it, and then provides for tools to interpret these modes. Using these tools, I have tried to understand the underlying physics. I have also identified similarities with other decompositions of the same data.

Before this could be done the algorithm was implemented in GNU Octave and tested for the system of a flow inside a cavity, in order to provide knowledge of the method and fine tune the algorithm. The required data for the flow inside a cavity was obtained using the program OpenFOAM [4].

The thesis is organized as follows: in the second chapter I make a general introduction to the physical system of Earth core flows involved in the geodynamo. In the third chapter I introduce the dynamic mode decomposition method. The fourth chapter is about the implementation of the algorithm in the test case of the flow inside a cavity. The fifth chapter shows the implementation of the code and results for Earth's outer core flow, and finally in the sixth chapter I draw some conclusions.

Chapter 2

Earth core flows

In this chapter the physical system to study will be described: the flow of molten iron in the Earth's outer core, located between 2900km and 5100km below the surface (see figure 2.1).

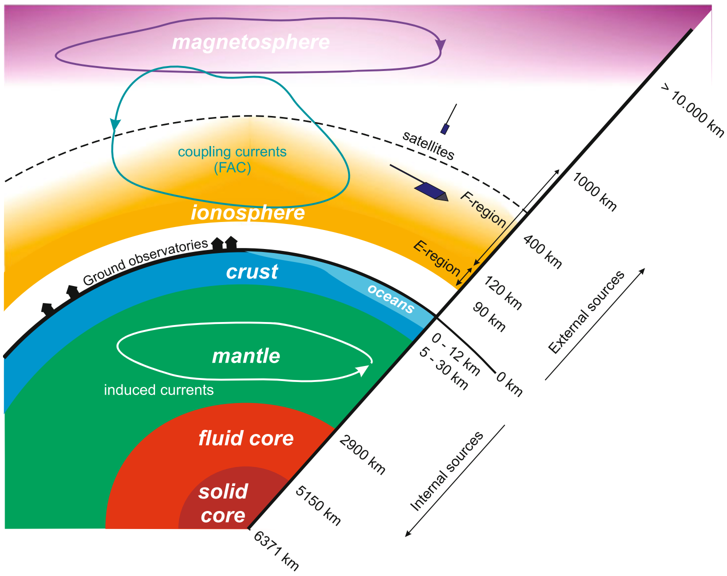

Figure 2.1: Representation of the different layers of the Earth and closer layers of the atmosphere [13].

2.1 The geodynamo

As a consequence of the Earth's rotation around its axis and physical forces inside the fluid (mainly buoyancy, Lorentz and pressure forces), the movement of the molten metal is complex, it does not simply flow around the solid inner core, it has many different aspects, which is why it is possible to maintain the magnetic field that we presently have.

The Earth's outer core flow system can be studied making use of the Magnetohydrodynamic (MHD) equations. MHD is a field of physics introduced by Hannes Alfvén for which he would later win the Nobel Prize in Physics in 1970. The equations used in MHD are constructed making considerations from both fluid dynamics and electromagnetism.

Starting from the fluid dynamics equations (mass conservation (2.1) and momentum conservation in its simplest form (2.2)), adding the contribution of the electromagnetic forces (Lorentz force), of gravity (buoyancy), of viscosity and of inertial forces due to the rotation of the reference frame, one can obtain equation 2.3 (see appendix A), the so called Navier-Stokes equation.

$$\frac{\partial \rho}{\partial t} + \nabla \cdot (\rho \vec{u}) = 0 \tag{2.1}$$

$$\rho \frac{\partial \vec{u}}{\partial t} = -\nabla p \tag{2.2}$$

$$\rho \left(\frac{\partial \vec{u}}{\partial t} + \vec{u} \cdot \nabla \vec{u} \right) + 2\rho(\vec{\Omega} \times \vec{u}) = -\nabla p + \vec{j} \times \vec{B} + \rho' \vec{g} + \mu \nabla^2 \vec{u} + \vec{f} \tag{2.3}$$

Where ρ is the hydrostatic density, $\vec{u}$ is the flow velocity, p is the non-hydrostatic part of the pressure, $\vec{\Omega}$ ($\vec{\Omega} = \Omega \hat{z}$) is the Earth's rotation vector, $\vec{j}$ is the current density, $\vec{B}$ is the magnetic field, ρ' is the departure from the hydrostatic density (ρ), $\vec{g}$ is the gravitational acceleration, ν is the kinematic viscosity and $\vec{f}$ accounts for other forces which may vary according to the considerations made about the system.

The term $\vec{j}\times\vec{B}$ on the right-hand-side of equation 2.3 is called the Lorentz force, and it reflects the interaction between the magnetic field and the flow of the electrically conductive fluid. It can be expanded, by making use of Ampère's law, equation 2.4, where the displacement current term was not included, for it is negligible for non-relativistic velocities.

$$\mu_0\vec{j} = \nabla \times \vec{B} \tag{2.4}$$

The Lorentz force term can then be written as in equation 2.5.

$$\vec{j} \times \vec{B} = \frac{(\vec{B}\cdot\nabla)\vec{B}}{\mu_0} - \nabla\left(\frac{B^2}{2\mu_0}\right) \tag{2.5}$$

Where on the right-hand-side is the magnetic tension force (first term) and the magnetic pressure force (second term).

The magnetic field is maintained by the geodynamo mechanism, in which the flow in the outer core, being an electrically conductive fluid because it is composed mainly by iron and nickel, generates a magnetic field. This process can be explained by the induction equation (2.11). Together with the Navier-Stokes equation (2.3), the induction equation (2.11) is another important contribution for the MHD system of equations, as they together define the dynamic problem. The induction equation can be deduced as follows:

Using equation 2.4 and Ohm's law (equation 2.6), one can write equation 2.7.

$$\vec{j} = \sigma(\vec{E} + \vec{u} \times \vec{B}) \tag{2.6}$$

$$\vec{E} = -\vec{u} \times \vec{B} + \frac{1}{\mu_0\sigma}\nabla \times \vec{B} \tag{2.7}$$

Where $\vec{E}$ is the electric field and σ is the electrical conductivity.

Introducing equation 2.7 into the Faraday's law equation (equation 2.8) we can write equation 2.9.

$$\frac{\partial \vec{B}}{\partial t} = -\nabla \times \vec{E} \tag{2.8}$$

$$\begin{aligned} \frac{\partial \vec{B}}{\partial t} &= \nabla \times (\vec{u} \times \vec{B}) - \frac{1}{\mu_0 \sigma} \nabla \times (\nabla \times \vec{B}) \\ \frac{\partial \vec{B}}{\partial t} &= \nabla \times (\vec{u} \times \vec{B}) + \frac{1}{\mu_0 \sigma} (\nabla^2 \vec{B} - \nabla(\nabla \cdot \vec{B})) \end{aligned} \tag{2.9}$$

With the Gauss's law for magnetism (equation 2.10) where the divergence of the magnetic field is zero, the last term on the right-hand-side of equation 2.9 is also zero, leaving us with equation 2.11, the induction equation.

$$\nabla \cdot \vec{B} = 0 \tag{2.10}$$

$$\frac{\partial \vec{B}}{\partial t} = \nabla \times (\vec{u} \times \vec{B}) + \eta \nabla^2 \vec{B} \tag{2.11}$$

Where η is the magnetic diffusivity ($\eta = (\mu_0 \sigma)^{-1}$).

The first term on the right-hand-side is an advective term, responsible for maintaining the magnetic field due to the flow's motion, and the second term is a dissipative term, which accounts for the loss of energy of the field.

Besides the fluid motion generating the magnetic field, if the magnetic field is strong enough it can affect the motion of the fluid (see equation 2.3), which is the case of the Earth's dynamo.

2.2 Observations on core flows

To use the dynamic mode decomposition method, data needs to be gathered about the motion of the fluid, but this is not an easy task because of the

depth inside the Earth where the core lies. There is no direct way to measure the velocity in the core, we have to obtain it indirectly, this is done by inverting data from the geomagnetic field that the flow produces. One uses the values of the geomagnetic field at the surface to calculate the flow in the core that created that magnetic field.
One of the problems is that the geomagnetic field we can observe at the surface is the superposition of many sources [13], some of them due to the Sun-Earth electromagnetic interaction and it can be difficult to isolate the contribution that originates only from the core. As we can see in figure 2.1 there are currents in the ionosphere and magnetosphere that generate their own contributions to the geomagnetic field. Also, induced currents in the Earth's crust and mantle can also contribute and even magnetised materials in the crust can affect measurements of the geomagnetic field. There are some ways to minimise the external and the internal non-core contributions which will not be discussed here.

Measurements are taken from onboard ships, in magnetic observatories and most recently from satellites. After a selection of the data, to minimise the contributions of sources others than the core, models can be created to represent the magnetic field. Once we have the geomagnetic field models, these are inverted to retrieve information about the outer core flow.

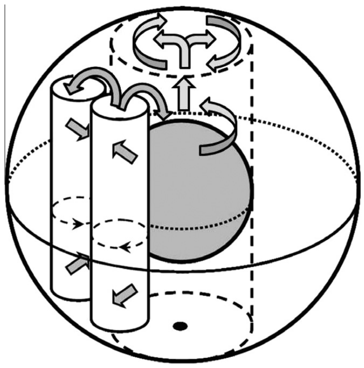

Figure 2.2: Structure of the flow in the outer core considering a quasi-geostrophic approximation. Columnar flows parallel to the rotation axis, the broken lines outline the tangent cylinder [3].

To invert the models, some a priori considerations have to be made about the flows in the outer core, and for this work the flow is considered to be quasi-geostrophic, as shown in figure 2.2. The flow is aligned in columns parallel to the rotation axis of the Earth, this is a consequence of a balance between the Coriolis force and the pressure gradient inside the core (see appendix A).

In this work, data from two different models of the geomagnetic field were used, they were the GUFM model [8] for the period of 1840-1990 and the COV-OBS model [5] for the period of 1840-2010. They were chosen for the large time period they represent. For the later years, the COV-OBS model uses satellite data, but even for the period for which we have data for both models, the models are different, because the methods used to compute them are different (but we will not discuss those methods here).

Chapter 3

DMD - formalism

The method of dynamic mode decomposition (DMD), proposed by Peter J. Schmid [19], is simply understood as a way of separating different flow components, hopefully due to different sources of motion that determine the fluid dynamic behaviour. More thoroughly, it enables one to study complex systems, where many different forces and dynamics act, and it allows the identification of areas of interest where relevant dynamics occur. This might be sources of disturbance, cyclic behaviour of the system, or other components that one can then try to associate with a physical phenomenon. It does this by decomposing the complex system in a series of modes, each capturing a different aspect of the overall dynamics.

Having these different modes allows one to recreate the original system, either exactly by using all the modes obtained or removing disturbance-related modes and showing a stabler version of the system. It is also possible, to some extent, to predict the future behaviour of the system in study using the dynamic modes, if careful attention is taken when selecting the modes so that disturbances do not overtake the system.

The greatest advantage in using this method over other possible methods, is the fact that the DMD does not require any knowledge about the dynamics of the fluid in study, that is to say, one does not need to know the physical equations that govern the system. If the system in study is obtained by numerical simulation, the prognostic equations are known and this is of no consequence. But when utilising experimental data, measured in a real system, one does not have this information, all that is available is the data we can observe, and the DMD method requires only this data.

3.1 Basic equations

First one needs sequences of data, snapshots of the system at regular intervals of time. Any aspect of the system can be studied, be it either velocity, intensity, density, or any other. For the purposes of this work, the scalar field of the stream function values was used, and later converted into velocity charts to represent the fluid's motion (see appendix A). This is possible for two dimensional incompressible flows.

Each of the snapshots is described by stream function values at M grid points, arranged into a vector v_i (equation 3.1). If one has N snapshots, there will be a total of N vectors, evenly spaced in time, by an interval dt.

$$v_i \quad ; \quad i = 1, 2, 3, \ldots, N \tag{3.1}$$

These N vectors are now concatenated to construct the matrix V_1^N $(M \times N)$, show in equation 3.2.

$$V_1^N = [v_1, v_2, v_3, \ldots, v_N] \tag{3.2}$$

This can be done using either numerical data, obtained via simulation or experimental data from observations.

Now the matrix A will be introduced, which is the matrix that regulates the evolution of the system. It can be obtained from the evolution equations of the system if numerical simulation results are used, but it is unknown when using experimental data. Despite this, the next steps will be done assuming this matrix exists and acts on the data as shown in equation 3.3.

$$Av_N = v_{N+1} \tag{3.3}$$

Considering two subsets of the matrix V_1^N, one where the last snapshot was removed (V_1^{N-1}) and the other where the first one was removed (V_2^N), as shown in equations 3.4 and 3.5, one can expand equation 3.3 into equation 3.6.

$$V_1^{N-1} = [v_1, v_2, v_3, \dots, v_{N-1}] \tag{3.4}$$

$$V_2^N = [v_2, v_3, v_4, \dots, v_N] \tag{3.5}$$

$$AV_1^{N-1} = V_2^N \tag{3.6}$$

For the purposes of this decomposition, one wants an expression that does not rely on the use of the matrix A. To achieve that, first the singular value decomposition (SVD) of the matrix V_1^{N-1} is done, as in equation 3.7.

$$V_1^{N-1} = U\Sigma W^T \tag{3.7}$$

Where the T denotes the transpose.

Now one has the matrix V_1^{N-1} written as a product of three others. The matrix U is an orthogonal square matrix with dimension $M \times M$ and has stored information about the spatial structures of the system, the matrix Σ is a rectangular diagonal matrix with dimension $M \times (N-1)$, and W is also an orthogonal square matrix with dimension $(N-1) \times (N-1)$, but this time with information about temporal structures of the system.

By inserting the singular value decomposition of matrix V_1^{N-1} into equation 3.6, one gets the next expression, equation 3.8.

$$AU\Sigma W^T = V_2^N \tag{3.8}$$

The term with the matrix A will now be isolated, starting from equation

3.8 and multiplying both terms by U^T on the left and $W\Sigma^{-1}$ on the right, where Σ^{-1} is the pseudo inverse of matrix Σ.

$$U^T A U \Sigma W^T W \Sigma^{-1} = U^T V_2^N W \Sigma^{-1} \tag{3.9}$$

From definition of unitary matrix W, one knows that $W^T W$ is equal to the identity matrix I, but $\Sigma\Sigma^{-1}$ is not, it only has diagonal elements , but not all equal to 1, the last values of the diagonal will be zero, this coming from the fact that Σ is a rectangular matrix. It will look similar to the matrix in equation 3.10 (if $M > N - 1$).

$$\Sigma\Sigma^{-1} = \begin{bmatrix} 1 & 0 & 0 & 0 & 0 & 0 \\ 0 & 1 & 0 & 0 & 0 & 0 \\ 0 & 0 & 1 & 0 & 0 & 0 \\ 0 & 0 & 0 & \ddots & \vdots & \vdots \\ 0 & 0 & 0 & \cdots & 0 & 0 \\ 0 & 0 & 0 & \cdots & 0 & 0 \end{bmatrix} \tag{3.10}$$

Knowing this an approximation will have to be done, which will be better the more snapshots are used in the creation of the matrix V_1^N, because they define the size of the matrix Σ and following that, the number of zeros in the diagonal of the matrix $\Sigma\Sigma^{-1}$. This approximation is shown in equation 3.11.

$$U^T A U \approx U^T V_2^N W \Sigma^{-1} \tag{3.11}$$

Note from equation 3.9 that, because $\Sigma\Sigma^{-1}$ is not the identity matrix, the right-hand-side of equation 3.11 involves a projection of A onto a subspace spanned by at most $(N - 1)$ columns of U. We can define a new matrix S:

$$S = U^T A U \tag{3.12}$$

Matrix S is an unitary transformation of A. It shares some properties with A that will allow one to obtain valuable information about the behaviour of the system, using only data from the snapshots provided, which normally would only be available by using A.

By combining equations 3.11 and 3.12 one gets the expression for the new matrix S, in equation 3.13.

$$S = U^T V_2^N W \Sigma^{-1} \tag{3.13}$$

The main goal with these steps is to obtain the dynamic modes, which will correspond to the eigenvectors of the matrix A. To this end, first the eigenvectors of matrix S will be calculated, for which the expression was obtained before and from them the modes will be derived.

$$S y_i = \mu_i y_i \quad ; \quad i = 1, \ldots, M \tag{3.14}$$

Equation 3.14 gives the eigenvectors (y_i) and eigenvalues (μ_i) of matrix S. Now the eigenvalues for matrix A will be obtained from equation 3.14, first by multiplying on the left by U and inserting $U^T U$, which is the identity matrix, into the left term.

$$U S U^T U y_i = U \mu_i y_i \tag{3.15}$$

From equation 3.12 one can easily see that $USU^T = A$, and so:

$$A U y_i = \mu_i U y_i \tag{3.16}$$

From equation 3.16 one can see that the eigenvectors of the matrix A are given by Uy_i, while the eigenvalues are the same as those for matrix S.
One can now define the dynamic modes as eigenvectors ϕ_i, where,

$$\phi_i = U y_i \tag{3.17}$$

and we can write from equation 3.16.

$$A \phi_i = \mu_i \phi_i \tag{3.18}$$

When analysing the dynamic modes, it is useful to define the dynamic spectrum, which is obtained by a logarithmic mapping of the eigenvalues, as in equation 3.19.

$$\lambda_i = \frac{\ln(\mu_i)}{dt} \tag{3.19}$$

The real part of λ_i provides information about the stability of the associated mode: if it is greater than zero it is unstable, near zero is stable and bellow zero represents modes that decay with time. The imaginary part represents the frequency of the mode [17] [19].

Information about the stability of the mode can also be retrieved directly from the eigenvalue μ_i. If the imaginary part is plotted against the real part of the eigenvalue, the points will loosely follow the contours of a circle of radius $|\mu_i| = 1$, with points outside being unstable (corresponding to the modes that increase exponentially with time), points inside corresponding to modes that decay over time and tend to disappear, and the ones on the circle or very close corresponding to stable modes. The advantage of using the dynamic spectrum to study the stability is an easier way to distinguish between stable and unstable modes.

Another aspect to take into consideration is the choice of the time interval dt between the snapshots. This can be any interval as long as there are enough snapshots to represent the system, for instance, if one were to have 20 snapshots, each separated by a time value of 1, one wouldn't choose $dt = 10$ for that would only give 2 snapshots to work with, and that would not be a very good representation of the system. There is also a fundamental inconvenience of using a too high dt value: this decreases the $(N-1)$ dimension of the subspace where matrix A is projected and as a result the approximation 3.11 may no longer be valid.

Besides the number of snapshots available, choosing different dt values can also affect the modes obtained. If a smaller dt is chosen, which means data is gathered with more frequency, the modes one will obtain in the end will correspond to higher frequency events, and most lower frequency ones will be interpreted either as noise, or mixed together into the mean mode.

If on the other hand one chooses a higher dt, lower frequency modes will emerge from the calculations, the steadier aspects of the flow will be shown, and the higher frequency ones will now be interpreted as noise.

This is easy to understand if one considers the available data for each set. More snapshots allow one to identify quicker events, events that otherwise one wouldn't have enough information to even know they happened, and by using fewer snapshots one can focus the attention on slower events, that because the more select number of snapshots become more evident, not having to be concerned with the higher frequency events.

3.2 Energy ranking and predictions

Decomposing a given flow into several modes, each representing a different component is useful in identifying the different dynamical sources behind observed behaviours, but something else that can be done is to use those modes to make predictions [12], to a certain degree, about the future behaviour of the system.

In order to recreate the flow from the dynamical modes one further needs to calculate the coefficients of the linear expansion, and sum the different modes taking into account their relative importance. This is done by making a projection of each mode onto the first snapshot v_1, as shown in equation 3.20. If we define Φ as the $M \times M$ matrix with eigenvectors ϕ_i as columns, then the vector $a = \Phi^{-1} v_1$ gathers the projections of v_1 onto different eigenvectors and:

$$a_i = (\Phi^{-1})_{ij}(v_1)_j \tag{3.20}$$

With these projection parameters, the norm associated with each mode can be defined as shown in equation 3.21. The norm of the modes, although not a proper energy by definition, will be referred also as the relative energy of the mode, as it allows to organise the modes by importance. Analysing the spectrum allows for a better selection of the relevant modes [18].

$$N = |a_i \phi_i| \tag{3.21}$$

To recreate any of the initial snapshots, equation 3.22 can be used.

$$v_k = \sum_{i}^{M} a_i \phi_i \mu_i^{k-1} \tag{3.22}$$

Where v_k is the snapshot one wants to obtain at time kdt, and μ_i is the eigenvalue i, k is the time index, it can be seen has advancing the system through the snapshots. Equation 3.22 is then the one to use for prediction. If one chooses for example $k = 1$, the first snapshot will be recreated, and so on, and these are perfectly obtained from the dynamic modes. If one chooses a value of k greater than the number of snapshots used, a snapshot of a prediction will be created, further away in time, but of course it has an error associated that grows the further we go.

From equation 3.22 there is a different definition of relative energy that can be obtained. The right-hand-side of the equation can be seen as the sum of all the modes with their relative contribution. If one takes just one of those terms and applies the initial idea, which was the norm of the dynamic mode together with the projection parameter, one can write equation 3.23.

$$N_k = |a_i \phi_i| |\mu_i|^{k-1} \tag{3.23}$$

It is similar to equation 3.21 but with the addition of the term containing the μ_i, which accounts for the stability of the mode. If k is chosen to be one, it equals equation 3.21, and this represents the initial norm of the mode. By choosing a different k, for a different time, the relative energy of that mode at that time is obtained. Modes with the eigenvalue located inside the circle of radius 1 will decay over time, so even if they have a big initial norm they will not be of big importance in the long run. On the other hand, modes with small initial norm that are unstable can grow to have big relative energies and overrun the system. It is important to analyse both aspects to have an idea of the importance of each mode, the initial norm ($N^{initial}$) and the final norm (N^{final}), which are obtained choosing $k = 1$ and k equal to the number of snapshots (N), respectively.

Chapter 4

DMD - testing

To implement the dynamic mode decomposition method, a code was written from scratch in GNU Octave. After some iterations and many problems solved, the final version can be found in Appendix B.

The tests of this algorithm were not applied to the Earth's liquid core system, but to a simpler one with well known dynamics, and for which results have been published [19] [20]. In this way mistakes could be easily spotted and corrections made.

The system chosen was the flow inside a square cavity, and the results of those tests are shown in the next section.

4.1 Flow inside a cavity

When a steady current flows over a cavity filled with liquid, a vortex starts to develop inside that cavity, and it is this system, shown in figure 4.1, that I will analyse.

To simulate this system and obtain the needed snapshots, an auxiliary program was used, OpenFOAM [4]. This program solves the Navier-Stokes equations to generate the different snapshots for the system in question.

The geometry chosen is shown in figure 4.1, a square cavity with three fixed walls, and no-slip boundary conditions, the top wall is moving at a

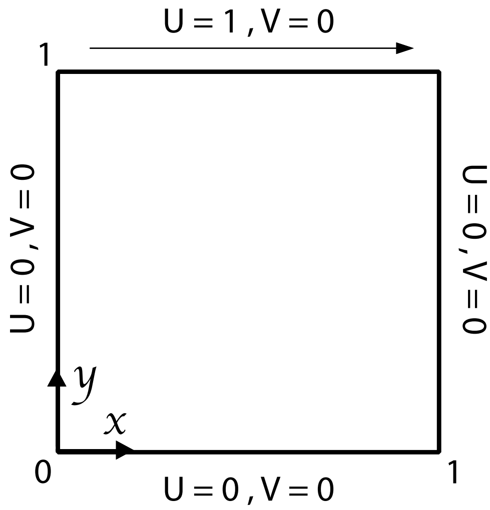

Figure 4.1: Flow over a cavity schematic. U represents the velocity in the x axis and V in the y axis.

constant speed to the right and the cavity is filled with a fluid with a certain viscosity (ν), providing an adjustable Reynolds number (Re), equation 4.1.

$$Re = \frac{UL}{\nu} \tag{4.1}$$

Where the U represent the relative velocity, L the characteristic length of the system and ν is the kinematic viscosity.

The stream function was calculated in a 50×50 grid inside the cavity, providing 2500 points per snapshot. The top lid velocity was set to $U = 1$, being all values provided adimensional, and the Reynolds number of 4500 was chosen for all the calculations shown here.

Figures 4.2(a) and 4.2(b) show the flow solution obtained for one of the snapshots from the OpenFOAM program, plotted as a vector field (left) and as the scalar of the stream function (right).

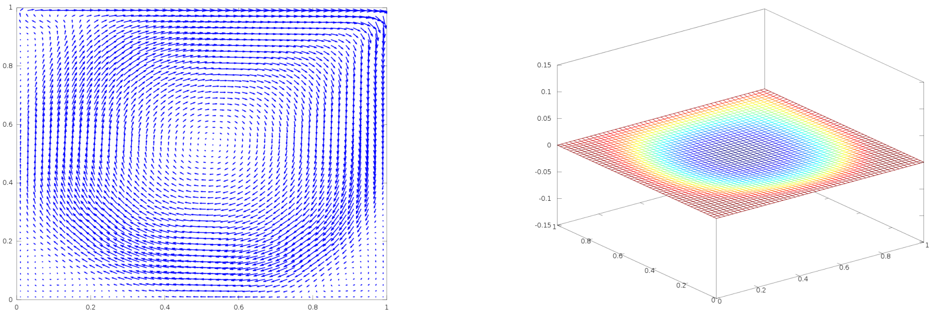

(a) (b)

Figure 4.2: Flow inside a 1x1 cavity with a moving lid with velocity 1, and a fluid with $Re = 4500$. (a) shows the vector field and (b) shows the stream function of the flow.

4.2 Results

OpenFOAM was used to generate 90 snapshots, regularly spaced in time with a time interval (dt) of 1, and then a matrix V_1^N was created with those snapshots. After applying the method described in chapter 3 the dynamic modes were obtained. The method generates M eigenvectors (2500 points each), but not all correspond to dynamic modes, first the relevant ones have to be selected.

Each eigenvector has a corresponding eigenvalue and only eigenvalues different from zero will give dynamic modes. This will give at most the minimum between M and $N-1$ modes if the properties of the $\Sigma\Sigma^{-1}$ matrix are taken into account.

After obtaining the dynamic modes one thing that can be done is to analyse the stability. There are some modes that reflect the stable behaviour of the system, but others represent the instabilities, the turbulent behaviour. This can be done by plotting the eigenvalues of each dynamic mode, the real part versus the imaginary, as in figure 4.3.

In light gray is represented a circle of radius 1. Points that fall outside this circle are considered unstable and grow over time and destabilise the system, points inside are damped and decay, and points on or near the circle are understood as stable, and maintain their behaviour more or less as the system evolves in time [10].

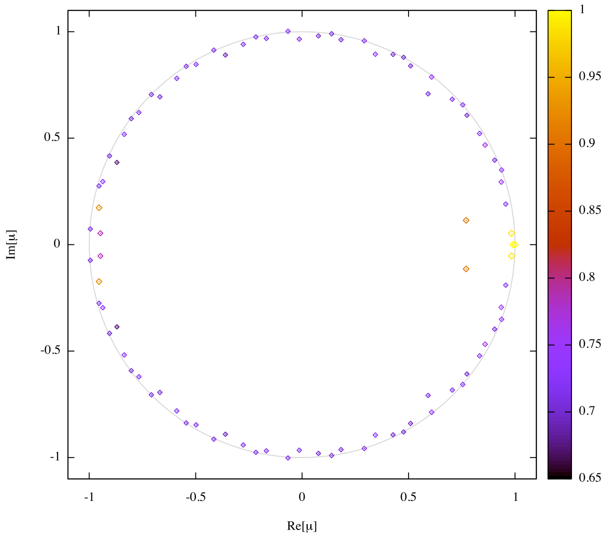

Figure 4.3: Plot of real part of eigenvalues versus imaginary part. 90 snapshots used and $Re = 4500$. Color and size coding by norm of corresponding mode.

There is an obvious symmetry along the y-axis, and that is because all the modes that have an imaginary part different from zero have a complex conjugate. Those with imaginary part zero are located in the zero line of the y-axis, so the symmetry is always observed.

Each point has a different colour and size, this is proportional to the relative energy of each mode, which is calculated as in equation 3.21, but in this initial test no projection was made so it simplifies to $N = |\phi_i|$.

As previously said in chapter 3, another way to determine the stability of the dynamic modes is by calculating λ, using equation 3.19.
This time the imaginary versus the real components will be plotted, and the stable modes will be the ones on the zero line, and the unstable ones above

it, as shown in figure 4.4.

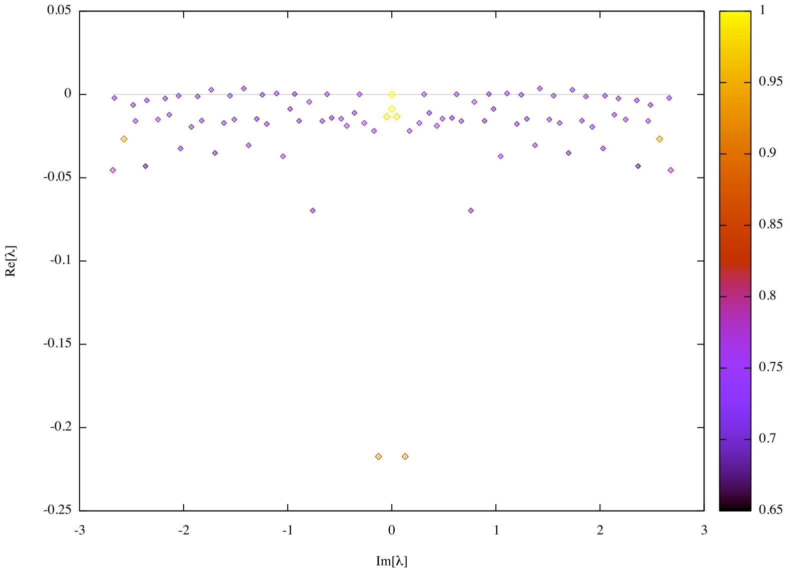

Figure 4.4: Plot of the dynamic spectrum, imaginary part of λ versus real part. 90 snapshots used and $Re = 4500$. Color and size coding by norm of corresponding mode.

The norm of the dynamic mode sets its relative importance against the other modes. In figure 4.5 one can see the imaginary part of the dynamic spectrum, or as said before the frequency of the mode, which from now on we will call ω, against the norm of the mode, or relative energy.
The normalisation of the energy comes from the method of calculating the dynamic modes, it is a consequence of the process.

The most energetic mode is the one with zero frequency, this is associated with the mean mode of the flow. A frequency of zero corresponds to an infinite period, from the equation $T = \frac{2\pi}{\omega}$.

From the 90 snapshots used in this test I obtained 88 dynamic modes, some are represented below, in figures 4.6, 4.7 and 4.8. The corresponding values of λ are shown in table 4.1, representing the stability of the mode, by the real part of λ and its frequency by the imaginary part of λ ($\lambda = \lambda_r + i\lambda_i$).

The selected modes are not the ones with greatest norm, they were chosen according to frequency, both high and low frequency, together with the zero frequency modes. This because at this time the norm calculated was not the best way to select the modes.

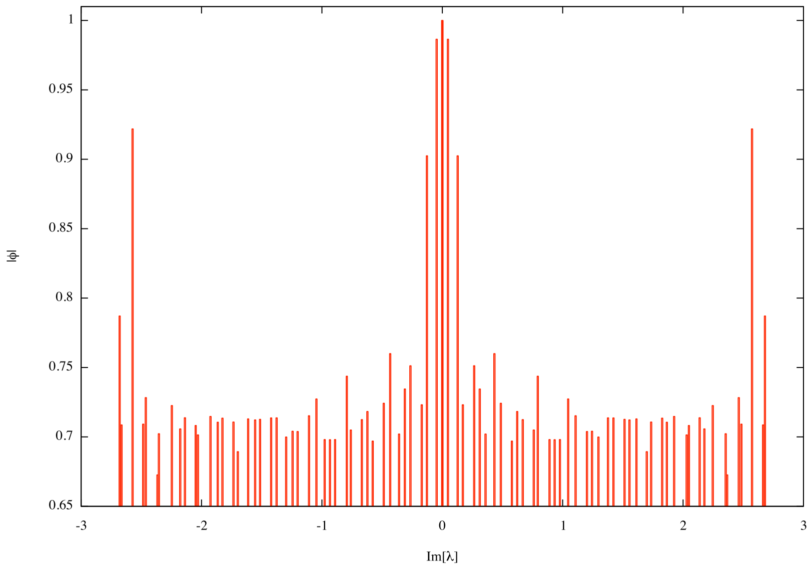

Figure 4.5: Plot of the relative energy of each mode, versus the frequency ω of the mode. The energy values are normalised to 1.

Modes	λ_r	ω
4.6(a) & 4.6(b)	-0.0000038	0.0
4.6(c) & 4.6(d)	-0.0086285	0.0
4.7(a) & 4.7(b)	-0.0111008	0.35914
4.7(c) & 4.7(d)	-0.0158912	0.89608
4.8(a) & 4.8(b)	-0.0007453	1.55466
4.8(c) & 4.8(d)	-0.0021294	2.66447

Table 4.1: Dynamic modes λ values for 90 snapshots, $Re = 4500$, lid driven flow in cavity.

The two modes shown in figure 4.6 are the ones with zero frequency, which would indicate that one of them is the mean mode. The first one is the one associated with the mean mode, figures 4.6(a) and 4.6(b), because it reflects

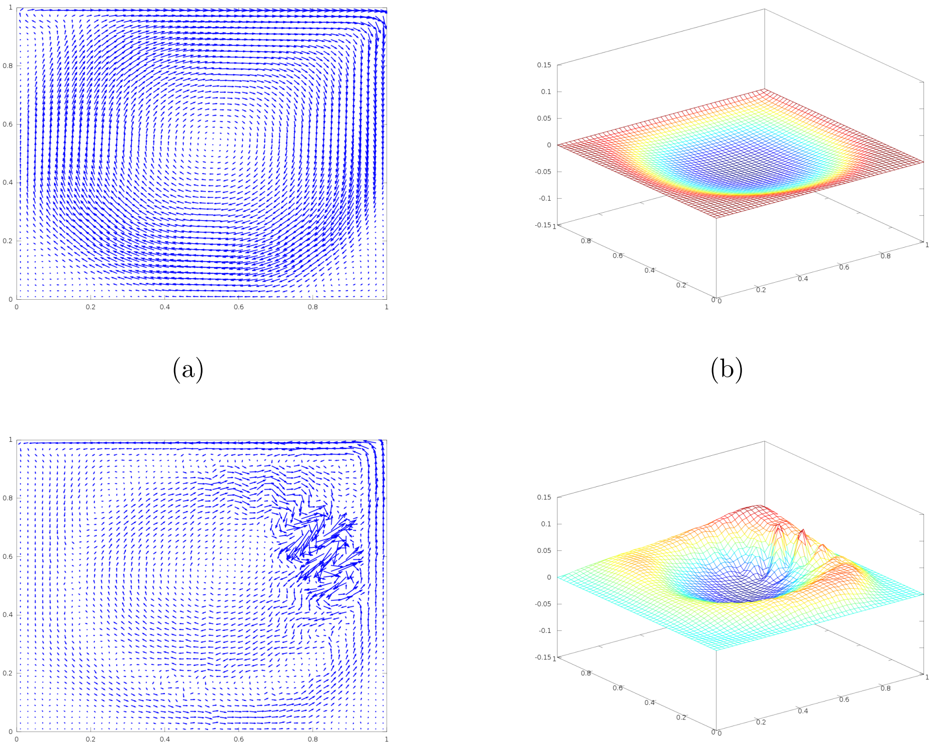

(a) (b) (c) (d)

Figure 4.6: Modes with zero frequency, the first (top) corresponds to the mean mode and the second (bottom) to turbulence. (a) and (c) vector field representation, (b) and (d) stream function representation

the spiral motion inside the cavity without any abnormal behaviour. This is the reason testing in a simple system is good, relations like these are easy to be spotted.

The other mode with zero frequency, figures 4.6(c) and 4.6(d), represents a turbulent behaviour, mostly located in the area where the movement of the top lid starts to force the fluid into a spiral flow. Despite the zero frequency, associated with a long lasting and underlying mode, this one either is very low in energy and not very relevant to the total flow or it decays very fast, not being of much importance in the long term.

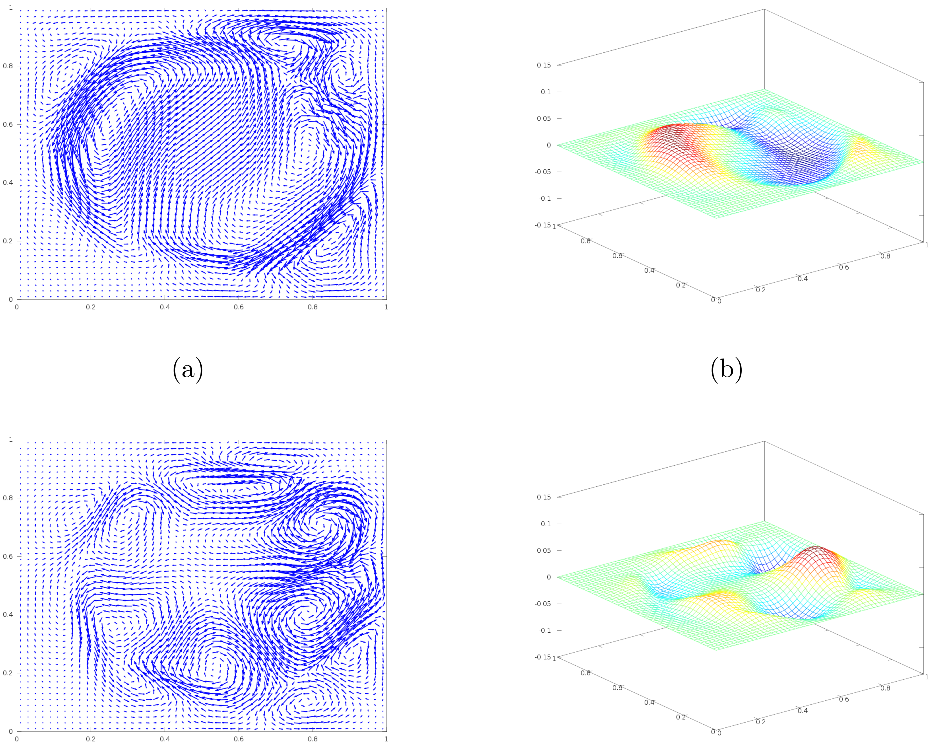

(a) (b)

(c) (d)

Figure 4.7: Modes with frequency 0.35914 (top) and 0.89608 (bottom). (a) and (c) vector field representation, (b) and (d) stream function representation

In figure 4.7 one can see two other modes from the same decomposition, they both show the circular movement in the cavity, with different intensities in different areas, but showing smooth behaviours. In figures 4.8(c) and 4.8(d) one can see that the circular movement is composed from small vortices, which show the underlying turbulence in the movement. In figures 4.8(a) and 4.8(b) this vortices are not visible in the entirety of the cavity, but only on the most turbulent area, as seen before in figures 4.7(c) and 4.7(d).

Figure 4.8 shows the last two modes from the decomposition that will be shown here, they show the turbulent aspect of the flow, it is clearly visible the vortices around the cavity, most strongly in the same upper corner near the moving wall.

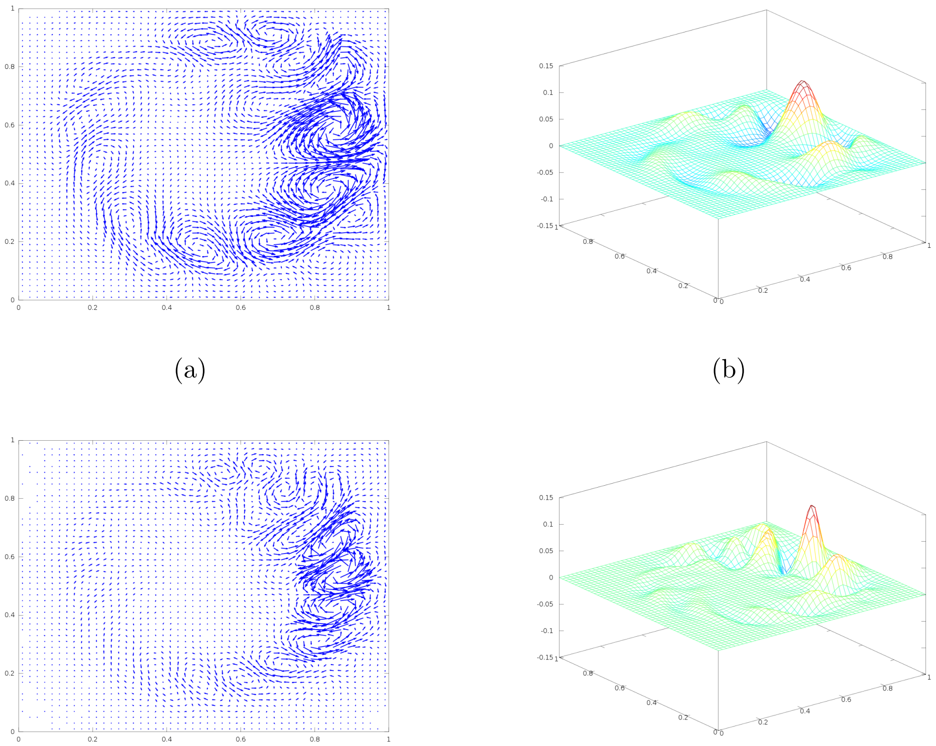

(a) (b)

(c) (d)

Figure 4.8: Modes with frequency 1.55466 (top) and 2.66447 (bottom). (a) and (c) vector field representation, (b) and (d) stream function representation

It is important to note that larger frequencies are associated with smaller scale features. Figure 4.6 shows the big scale features, with zero frequency, figure 4.7 shows smaller scale features with greater than zero frequencies, and figure 4.8 shows even smaller scale features corresponding to even higher frequencies.

This first decomposition was used as a test of the method. In the Earth core system, chapter 5, the method was much improved and more information about each individual mode was gathered and the relative importance of each one is better understood.

Chapter 5

DMD - application to Earth's core flows

In this section the results obtained by implementing the dynamic mode decomposition code in appendix B to the Earth outer core flow charts will be presented and interpreted, and also some explanation about the algorithm itself will be given.

5.1 'Data' for core flows

The data used for the study of the outer core flow of the Earth was provided by the output from inversions of two geomagnetic field models as previously said: the GUFM model for the period of 1840-1990 and the COV-OBS model for the period of 1840-2010.

The snapshots used for the study were grids of the core flow stream function for each year, amounting to 151 charts from the GUFM model and 171 from the COV-OBS model, but for the purpose of better comparing both models only the first 151 years of the COV-OBS model were used, using information from 1840 to 1990 for both models.

As discussed before in chapter 3 the choice of time interval (dt) is important, because different time intervals will give different results. As said before, too small dt values do not properly recover the longer periods and too large values lead to small values of N and a larger error in estimating A through equation 3.11.

For both data sets, time intervals from 1 yr to 20 yrs were used, to test for different behaviours. Using a time interval past 10 yrs did not provide very interesting results, because of the low number of snapshots I had to work with. In figures 5.1 through 5.10, the dynamic spectrum for the first 10 time intervals is shown, for both the GUFM model (red) and the COV-OBS model (green). In figures 5.1 and 5.2, the ones with $dt = 1$ and $dt = 2$ respectively, a large number of modes can be seen, as expected from a small time interval, but these are not ideal for the study done here because they show many unstable modes, both above and below the stability line ($Re[\lambda] = 0$). Also, with this choice of time interval, although it made use of the maximum information available, I could only see high frequency modes, the longer period ones (low frequency) were lost and blurred by the high frequency ones. The high frequency modes were commonly very chaotic, with many small scale structures.

The scale of the dynamic spectrum figures is the same for all time intervals, so the clear reduction in dynamic modes can be seen due to the increasing time increment, dt, and the relative stability of individual modes across figures can be seen. It is not so clear in figure 5.3 but it still represents a bad aggregation of modes, with many unstable ones. Figure 5.4 excluding a few damped modes, has most of the modes concentrated in the stability line. Both the time interval of 5 yrs (figure 5.5) and of 6 yrs (figure 5.6) also show for the most part stable modes. Figure 5.7 excluding one mode from the COV-OBS model, has all its modes very close to the stability line. Although with this time interval the amount of dynamic modes available is smaller, it still provides a good amount of information. Figure 5.8 still shows stable modes, but in increasingly smaller numbers. The last two time intervals shown, 5.9 and 5.10 even though they seem to represent stable modes, the small quantity of snapshots means that previously identifiable modes here are mixed, distorting the information that could otherwise be obtained.

For the most part, a reduction of unstable modes, above $Re[\lambda] = 0$ and fast decaying modes, below the same line, is observed the greater the time interval shown. By calculating too many modes, the method will generate unnecessary and unstable modes, by calculating fewer modes, the amount of unnecessary modes decreases and so we obtain a more accurate and stabler representation of the system. Of course, a balance must be found, otherwise our modes will begin to mix together and information will be lost.

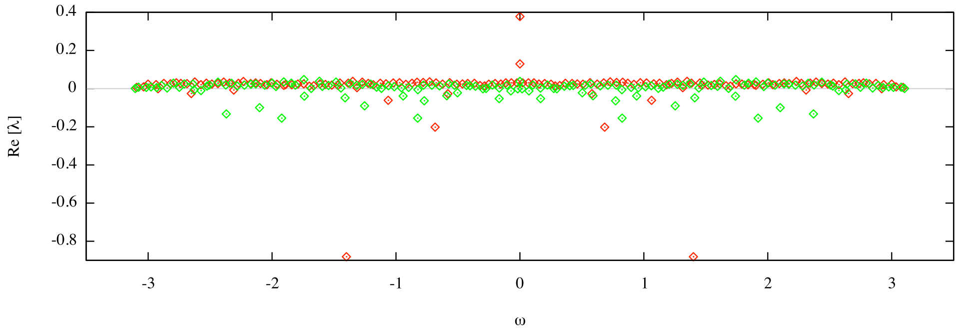

Figure 5.1: Dynamic spectrum for the time interval of 1 yr. The stability on the y-axis, frequency on the x-axis. In red the values for the GUFM and green the COV-OBS model.

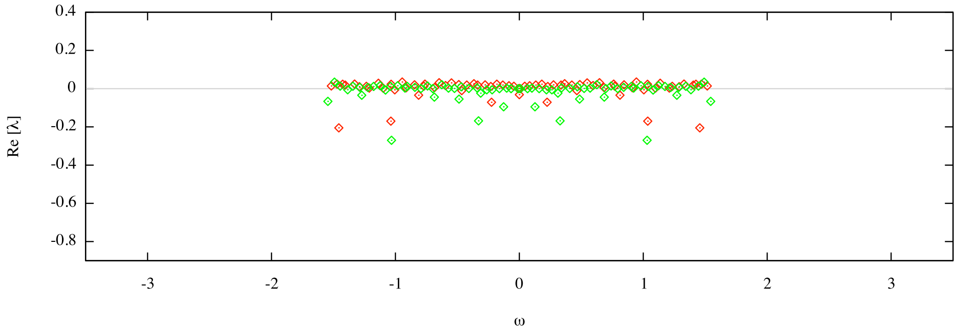

Figure 5.2: Dynamic spectrum for the time interval of 2 yrs. The stability on the y-axis, frequency on the x-axis. In red the values for the GUFM and green the COV-OBS model.

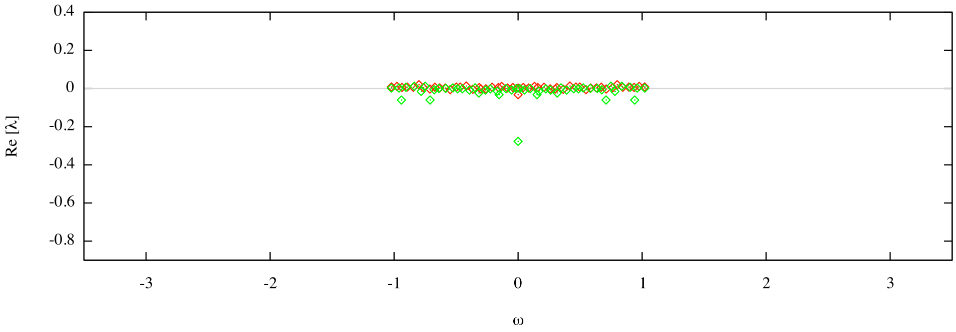

Figure 5.3: Dynamic spectrum for the time interval of 3 yrs. The stability on the y-axis, frequency on the x-axis. In red the values for the GUFM and green the COV-OBS model.

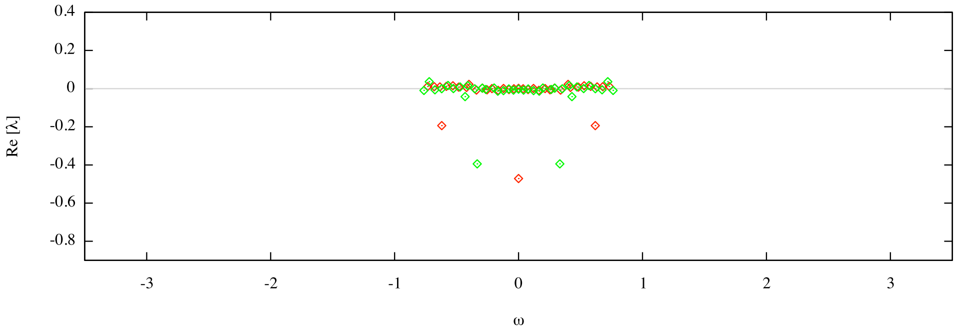

Figure 5.4: Dynamic spectrum for the time interval of 4 yrs. The stability on the y-axis, frequency on the x-axis. In red the values for the GUFM and green the COV-OBS model.

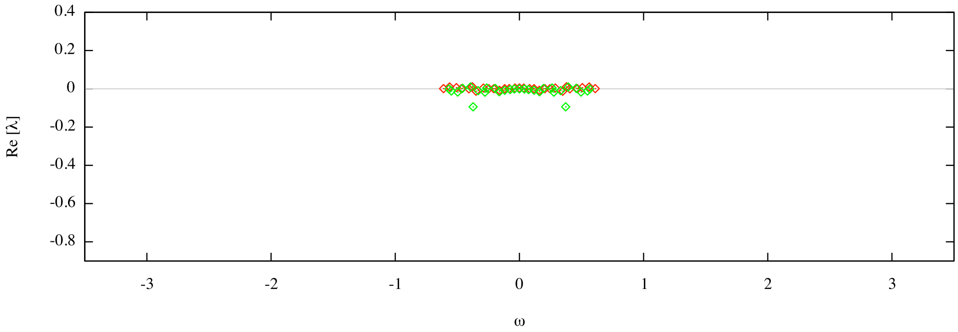

Figure 5.5: Dynamic spectrum for the time interval of 5 yrs. The stability on the y-axis, frequency on the x-axis. In red the values for the GUFM and green the COV-OBS model.

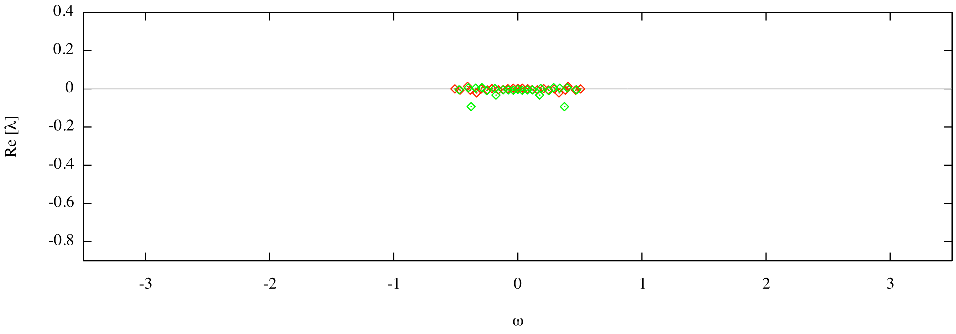

Figure 5.6: Dynamic spectrum for the time interval of 6 yrs. The stability on the y-axis, frequency on the x-axis. In red the values for the GUFM and green the COV-OBS model.

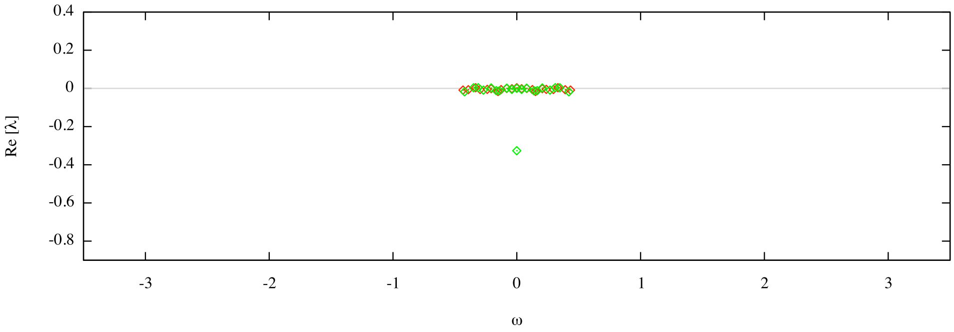

Figure 5.7: Dynamic spectrum for the time interval of 7 yrs. The stability on the y-axis, frequency on the x-axis. In red the values for the GUFM and green the COV-OBS model.

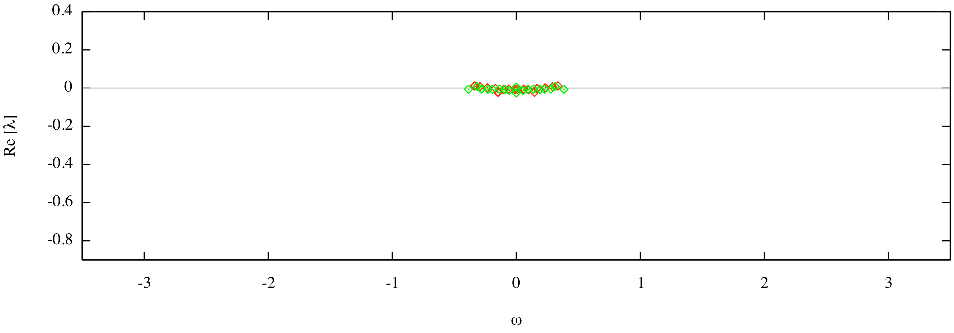

Figure 5.8: Dynamic spectrum for the time interval of 8 yrs. The stability on the y-axis, frequency on the x-axis. In red the values for the GUFM and green the COV-OBS model.

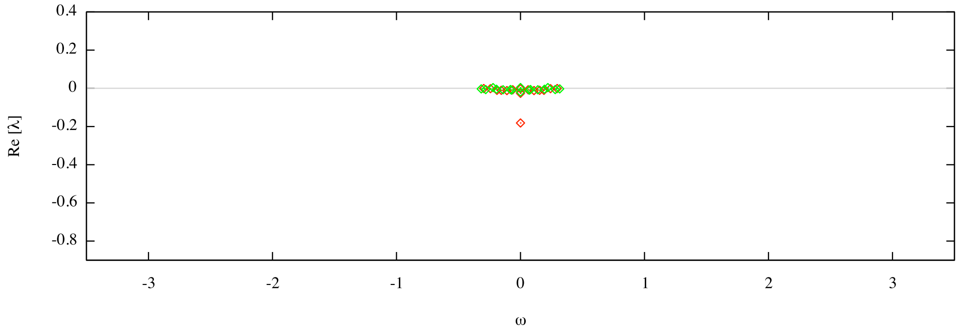

Figure 5.9: Dynamic spectrum for the time interval of 9 yrs. The stability on the y-axis, frequency on the x-axis. In red the values for the GUFM and green the COV-OBS model.

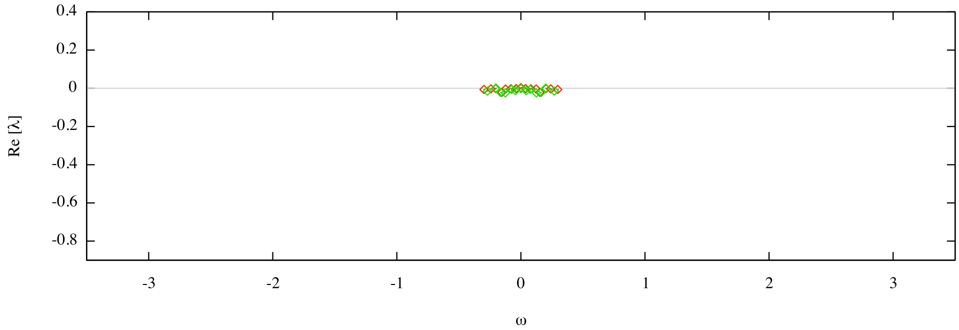

Figure 5.10: Dynamic spectrum for the time interval of 10 yrs. The stability on the y-axis, frequency on the x-axis. In red the values for the GUFM and green the COV-OBS model.

After my tests, two time intervals were identified as giving similar results between them and showing correspondence to results from Principal Component Analysis (PCA) [15]: these were $dt = 4$ yrs and $dt = 7$ yrs, and those are the ones that will be shown below.

5.2 Results

5.2.1 Time interval of 4 yrs

Table 5.1 shows approximately half of the dynamic modes obtained in the decomposition for the GUFM model with a time interval of 4 yrs. This is because for each mode associated with a complex eigenvalue, the method also generates another mode associated with an eigenvalue which is the complex conjugate of the previous one. In the end we have two modes with the same aspect, same real λ_r but symmetric imaginary component ω. Those with zero imaginary component of eigenvalue λ_i, only appear once and normally represent the mean modes.

In the next tables as 5.1, the quantity 'stability' is the real part of λ given by equation 3.19 (λ_r). It's unsigned reciprocal has the meaning of a mean lifetime for negative and e-folding time for positive values of λ_r. The closer the 'stability' value is to zero, the stabler the mode is (the mean lifetime tends to infinity). The frequency is the imaginary part of λ (ω), and the period is obtained simply by doing $T = \frac{2\pi}{\omega}$. Finally the norm (N) is obtained from equation 3.23.

There are three different dynamic modes that I will analyse in this work, and those are the ones shown in bold on the different tables. They are the top three modes in relative energy (norm) if the final norm (N^{final}) is used. Although not shown here, they are the top three modes in this energy ranking for most of the time intervals tested, so they are the ones that I will focus my attention on.

The first one in table 5.1 is a zero frequency mode, which means an infinite period. This mode can be associated with the mean flow. The two next modes have more complicated explanations for their behaviour that will be given ahead in this chapter. Even though they are the top three modes in the energy ranking chosen for table 5.1, that is not always the case, as can be seen in table 5.3.

An important parameter to take into account here is the period of the modes.

Analysing tables 5.1 and 5.2 we can see that for a time interval of 4 yrs, both in the GUFM and in the COV-OBS models we get one mode with a period of around 80 yrs and another of around 160 yrs. They do not appear in the same order for both models, on the GUFM model the $\sim$ 160 yrs mode is second and the $\sim$ 80 yrs is third and on the COV-OBS model it's the other way around. This is not so relevant as the fact that they are the most energetic modes as a group.

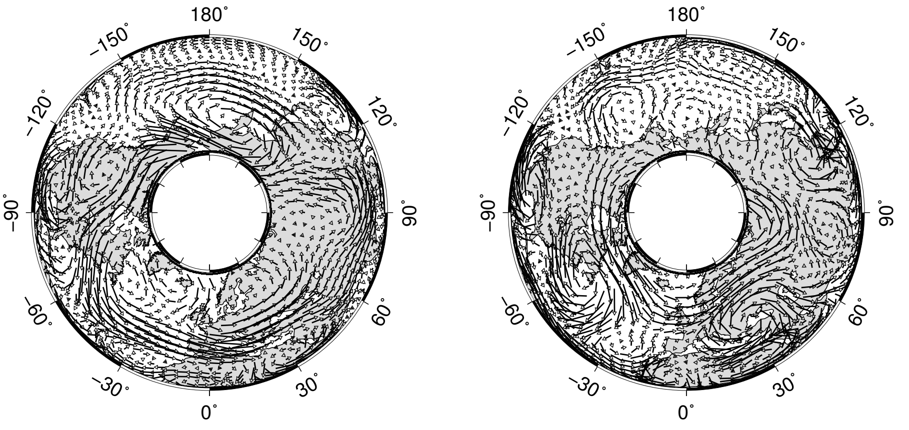

(a) T = ∞

(b) T = 81.45 years

Figure 5.11: Vector field representation of two dynamic modes from the GUFM model decomposition with a time interval of 4 yrs.

Figure 5.11 shows two examples of modes (also depicted in figure 5.12) from the decomposition of the flows inverted from GUFM, specifically the mode with infinite period on the left and the mode with a period of 81.45 years on the right.

These charts were obtained by using the stream function to generate the vectors of the fluid's flow (see appendix A). Despite indicating the direction in which the fluid moves in the surface of the outer core (to whitin the algebraic sign), the images are hard to interpret and compare to others. That is why only the two modes in figure 5.11 will be shown in this manner and all others using the stream function, which is much easier to analyse and identify the different structures.

In table 5.3 both models are represented in order to show the difference in choosing a different energy ranking. In this case equation 3.21 was used (corresponding to the energy distribution in the initial epoch) and it can be seen for example that in the GUFM case the second most energetic mode is also one with zero frequency, the same as the mean mode, but in this case

Stability	$Frequency(years^{-1})$	$Period(years)$	N^{final}
0.001399	**0.000000**	∞	**71.782424**
-0.000663	**0.037520**	**167.463861**	**17.469653**
-0.005036	**0.077140**	**81.451726**	**11.954881**
0.022269	0.399991	15.708310	9.429898
0.000892	0.120996	51.928821	8.804339
0.000171	0.214329	29.315584	4.457206
0.006240	0.419349	14.983180	3.840010
-0.008928	0.164022	38.307037	3.723223
0.014806	0.528952	11.878553	3.587201
0.002648	0.290993	21.592225	3.465212
0.007930	0.482869	13.012191	2.856919
0.011719	0.582143	10.793197	2.634215
-0.006251	0.253894	24.747322	2.346580
0.011158	0.732069	8.582777	1.926278
0.009014	0.634562	9.901610	1.743119
0.010086	0.679963	9.240486	1.715047
-0.007775	0.339400	18.512618	1.306748
-0.193993	0.619393	10.144104	0.000000
-0.471241	0.000000	∞	0.000000

Table 5.1: Dynamic modes with $\mu_i \neq 0$ for the GUFM model and time interval of 4 yrs. Stability, frequency, period and final norm, from equation 3.23 for each mode.

it is not a relevant mode because it's energy rapidly decays, as can be seen comparing with table 5.1 which shows the energies at the final epoch of the snapshots time range, while in tables 5.3 the initial energy is shown.

Depending on the purposes of the study, it may be more significant to account for the energy in the initial stage of the system, for others, in the final stage. I will study here the modes already identified, ranked by the final norm.

In figure 5.12 the three modes for both models that were highlighted before are shown side by side for comparison between them. The stream function is used to represent the flow, and a view from the north pole is used in an orthographic projection.

Stability	$Frequency(years^{-1})$	$Period(years)$	N^{final}
-0.002840	**0.000000**	∞	**50.946225**
-0.001573	**0.078230**	**80.317332**	**15.470077**
-0.007911	**0.040645**	**154.586917**	**10.307104**
0.003265	0.196369	31.996883	10.049713
0.036163	0.720273	8.723333	6.624580
0.002675	0.292175	21.504870	5.738887
0.015659	0.408708	15.373298	5.616980
-0.010304	0.121251	51.819445	4.703794
0.016493	0.568536	11.051510	4.549433
0.008839	0.471360	13.329902	3.815228
-0.004289	0.263599	23.836129	3.044376
-0.013371	0.167001	37.623603	2.908860
-0.000997	0.353026	17.798064	2.568605
0.000241	0.525481	11.957025	1.753703
-0.000372	0.619569	10.141215	1.110994
-0.006300	0.674183	9.319699	0.698976
-0.009563	0.762946	8.235423	0.529885
-0.041797	0.430931	14.580497	0.028705
-0.394328	0.333149	18.859969	0.000000

Table 5.2: Dynamic modes with $\mu_i \neq 0$ for the COV-OBS model and time interval of 4 yrs. Stability, frequency, period and final norm, from equation 3.23 for each mode.

To generate the flow charts used in this work, the Generic Mapping Tools (GMT) software was used. It is very widely used for generating maps and projection of different geophysical fields on the Earth's globe. The hole in the center of the projections is there because the QG assumption used to derive the flow information does not work well in the regions above and below the solid inner core, known as tangent cylinder [3]. For this reason only data from latitudes of $-70°$ to $70°$ are used. In figures like 5.12 only the core flow modes over the northern hemisphere are shown, but due to symmetry in relation to the equator they characterise the whole flow. This is clearly seen in figure 5.13.

It is clear in figure 5.12 that the modes have not exactly the same spatial structure for both models, but all the key features are the same. For the infinite period modes, the colours are switched, but that is merely a multiplication by a factor of -1 that is compensated by the sign in a_i (see equation 3.22) on the data set, and it is not relevant.

$Period(years)$	$N^{initial}$	$Period(years)$	$N^{initial}$
∞	**133.160235**	18.859969	272.748821
∞	58.354511	∞	**77.567043**
10.144104	30.060183	**154.586917**	**33.237421**
81.451726	**25.189171**	51.819445	21.613331
167.463861	**19.269553**	37.623603	21.045807
38.307037	13.956136	**80.317332**	**19.524163**
51.928821	7.715992	14.580497	13.948146
24.747322	5.918492	31.996883	6.198941
29.315584	4.345507	23.836129	5.743337
18.512618	4.130080	21.504870	3.862480
21.592225	2.341853	17.798064	2.976997
14.983180	1.524882	8.235423	2.181916
13.012191	0.883432	9.319699	1.775910
10.793197	0.464944	11.957025	1.692132
9.901610	0.459123	10.141215	1.173835
11.878553	0.400961	13.329902	1.031335
9.240486	0.385478	15.373298	0.553404
8.582777	0.369453	11.051510	0.396160
15.708310	0.349278	8.723333	0.031388

Table 5.3: Period and energy for modes of GUFM (left) and COV-OBS (right) for time interval of 4 yrs, ordered by their norm using the initial norm from equation 3.23

From [15], which analysed the same data sets we work with here, but did so using the Principal Component Analysis (PCA) method, it can be seen that similar modes emerged to those in figure 5.12, i.e., the mean flow (top) the $\sim$ 160 yr period mode (middle) and the $\sim$ 80 yr period mode (bottom). In [15] the mean mode was obtained by doing the average of all the snapshots, and so no dynamic information was obtained about it, but in my tests, it emerges as a dynamic mode of it's own, as a consequence of the decomposition. In this way I have information about the stability and behaviour of the mode, and it also serves to confirm that it is indeed the mean mode I obtained.

It is also worth noting that the PCA mode corresponding to the ~ 160 yrs periodicity in this study did not appear as being periodic with PCA.

The aspect of the mean flow mode can be explained by a combination of two mechanisms as explained in [2], where simulations of the Earth's geodynamo were made. First, a gravitational coupling between the inner core and the mantle, that forces the outer core flow into a rotating shell, providing a westward flow, close to the mantle. Second, a variation of the growth-rate of the inner core, causes an asymmetric thermal convection and an eccentricity of the jet. Both these effects, cause an eccentric westward gyre located beneath the Atlantic at low latitudes, and beneath the Pacific at high latitudes. As it is a QG structure, one can perceive where it is closest to the core surface. The mode's aspect in figures 5.12 and 5.15 reflects this behaviour.

The two other modes represented in figures 5.12 and 5.15 are also obtained by the method in [15]. From the PCA method a general time variation (not necessarily periodic) can be retrieved associated to a given mode, but the second mode obtained in [15] looks to have a periodicity of around 80 yrs, corresponding to what I obtain here for the dynamical mode shown at the bottom of figure 5.12. In fact, using DMD, a similar looking mode, with two vortices, around longitude $-60°$ and $30°$, and an opposite vortex around the tangent cylinder, is obtained and its period is also around 80 yrs, for the time increment of 4 yrs from table 5.3 and around 78 yrs for the time increment of 7 yrs from table 5.6.

The other mode that I show here has a period of around 160 years for most tests and it also appears in [15], although not associated with a periodic time function. The periodicity of this mode may not be a robust feature. It may be a consequence of the limited amount of information I have to analyse since the time interval I have at my disposal is 151 years, which more or less coincides with the found period.

Such a periodicity of ~ 160 yrs has however been recently found by other authors (Jackson and Mound,2010) [9], suggesting that it should be considered for further studies. Here, it could show a higher performance of DMD compared to PCA in extracting relevant superposed modes.

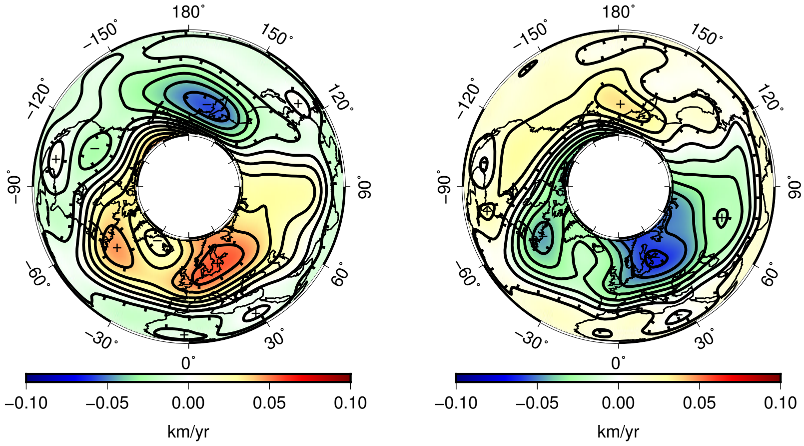

(a) T = ∞ (b) T = ∞

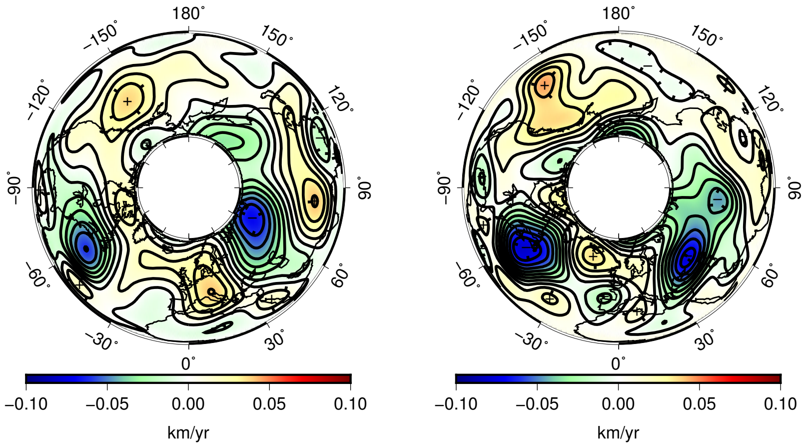

(c) T = 167.46 years (d) T = 154.59 years

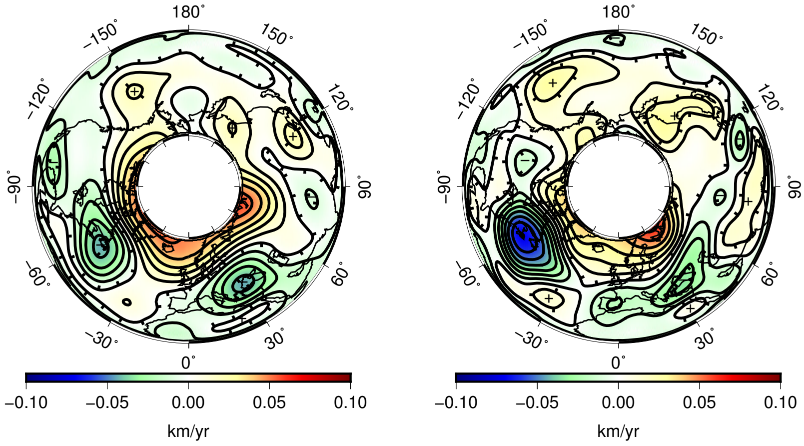

(e) T = 81.45 years (f) T = 80.32 years

Figure 5.12: Dynamic modes plotted as stream functions, in a view from the north pole, showing latitudes between 0° and 70°. GUFM model (left) and COV-OBS model (right) for a time interval of 4 yrs. Modes represented here are highlighted in tables 5.1 and 5.2.

5.2.2 Time interval of 7 yrs

The other case studied corresponds to choosing the time interval $dt = 7$ yrs, and as can be seen in figure 5.15 the modes are quite similar, with vortices around the same places, the small differences can be attributed to a different amount of data.

In tables 5.4, 5.5 and 5.6 the information about each mode referred above can be seen, and is much the same as the information in tables 5.1, 5.2 and 5.3 for the time interval of 4 yrs. In this case, the same information can be taken by using a different time interval, so no new interpretation comes from choosing $dt = 7$ yrs, but it is useful to see the similarities by choosing less data. Some modes will of course be different, but those are not shown here as they were not the focus of the study.

Stability	$Frequency(years^{-1})$	$Period(years)$	N^{final}
0.003439	**0.000000**	∞	**81.619565**
-0.000302	**0.080870**	**77.695197**	**17.105231**
-0.001818	**0.039103**	**160.68338**1	**16.231589**
-0.006386	0.126560	49.645834	6.708596
-0.001486	0.206426	30.437987	4.562660
0.003629	0.332522	18.895545	3.117376
-0.004913	0.238405	26.355132	2.846390
-0.016033	0.151689	41.421523	2.446380
-0.008786	0.434024	14.476573	2.237760
-0.005667	0.295641	21.252773	1.624948
-0.007021	0.391310	16.056786	1.617192

Table 5.4: Dynamic modes with $\mu_i \neq 0$ for the GUFM model and time interval of 7 yrs. Stability, frequency, period and final norm, from equation 3.23 for each mode.

As can be seen in the tables for $dt = 7$ yrs, there are less modes than for $dt = 4$ yrs, this is a consequence of the method, which as previously said will give at most the minimum between M and $N - 1$, depending on the eigenvalue associated to each mode. If an eigenvalue only has real part and if it is negative, the corresponding mode will not be considered. This is because the study of the stability and frequency of each mode requires a logarithmic mapping of the eigenvalues, and the values that are located on the negative real axis of the logarithm function aren't allowed, because there is a branch cut in that area [1].

Stability	$Frequency(years^{-1})$	$Period(years)$	N^{final}
0.000125	**0.000000**	∞	**59.702860**
0.000954	**0.080229**	**78.315392**	**16.915643**
-0.005323	**0.039165**	**160.428553**	**11.149480**
0.002391	0.206277	30.459913	8.473828
0.003584	0.310965	20.205427	5.674270
-0.012694	0.139735	44.965094	4.542461
0.003313	0.348265	18.041394	4.281917
-0.011943	0.165015	38.076485	4.131215
-0.009115	0.268775	23.377152	1.974457
-0.017978	0.420892	14.928252	0.751653
-0.326478	0.000000	∞	0.000000

Table 5.5: Dynamic modes with $\mu_i \neq 0$ for the COV-OBS model and time interval of 7 yrs. Stability, frequency, period and final norm, from equation 3.23 for each mode.

$Period(years)$	$N^{initial}$	$Period(years)$	$N^{initial}$
∞	**49.234557**	∞	440.807046
41.421523	25.829847	∞	**58.613617**
160.683381	**21.205237**	44.965094	29.357847
77.695197	**17.882747**	**160.428553**	**24.382634**
49.645834	17.151774	38.076485	23.907375
14.476573	8.141993	**78.315392**	**14.701343**
26.355132	5.860553	14.928252	10.561671
30.437987	5.676524	23.377152	7.539525
16.056786	4.539545	30.459913	5.962794
21.252773	3.737741	20.205427	3.350614
18.895545	1.828436	18.041394	2.631018

Table 5.6: Period and energy for modes of GUFM (left) and COV-OBS (right) for time interval of 7 yrs, ordered by their norm using the initial norm form equation 3.21

By choosing a time interval of 7 yrs there are also two modes with zero frequency, but this time in the COV-OBS model. The same behaviour can be seen, where for the initial epoch the two modes are at the top of the energy ranking, but looking at the final epoch, only one of them, coinciding with the mean flow from the PCA analysis, remains at the top and the other falls to zero energy. In table 5.5 it can be seen that the stability of this mode has the lowest negative value, which means it decays quite fast [10]. From the reciprocal of the 'stability' parameter, a decaying time of $\sim$ 3 yrs can be computed. This was also the case for the mode for the GUFM model in $dt = 4$ yrs, seen in table 5.1, where the decaying time was $\sim$ 2 yrs.

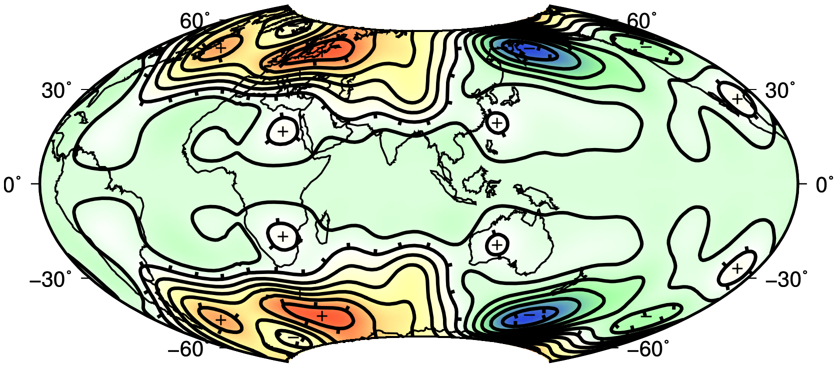

(a) T = ∞

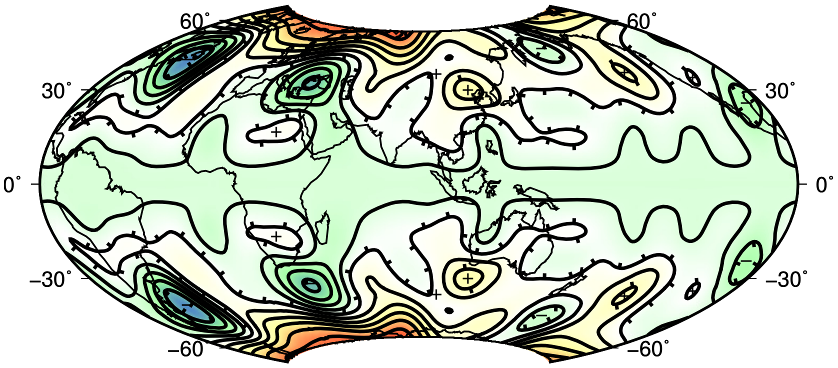

(b) T = 77.70 years

Figure 5.13: Dynamic modes plotted as stream functions, in a view from the equator, showing latitudes between −70° and 70°, and all longitudes. GUFM model for a time interval of 7 yrs.

In figure 5.13 a different view of the modes is given, centering the equator, and giving a vision of all the globe. The modes represented are from the time interval of 7 yrs for the GUFM model, the first from the top being the mean mode and the other the mode with period of 77.70 years. The symmetry about the equator can clearly be seen, which was imposed by the choice made when calculating the flows from the geomagnetic data.

Figure 5.14 shows the dynamic spectrum for the time interval of 4 yrs in the top and the interval of 7 yrs in the bottom, using red for the GUFM model and green for the COV-OBS model. It shows the same information that is on figures 5.4 and 5.7, but zoomed in so it can be more clearly seen. It can be seen that with the exception of a few modes they are all close to the zero line, which means they are more or less stable.

The modes with zero frequency and very negative λ_r in both graphics are the modes that appear to be mean modes but decay very fast over time, consequence of the real component of λ being so low, i.e., a short decaying time.

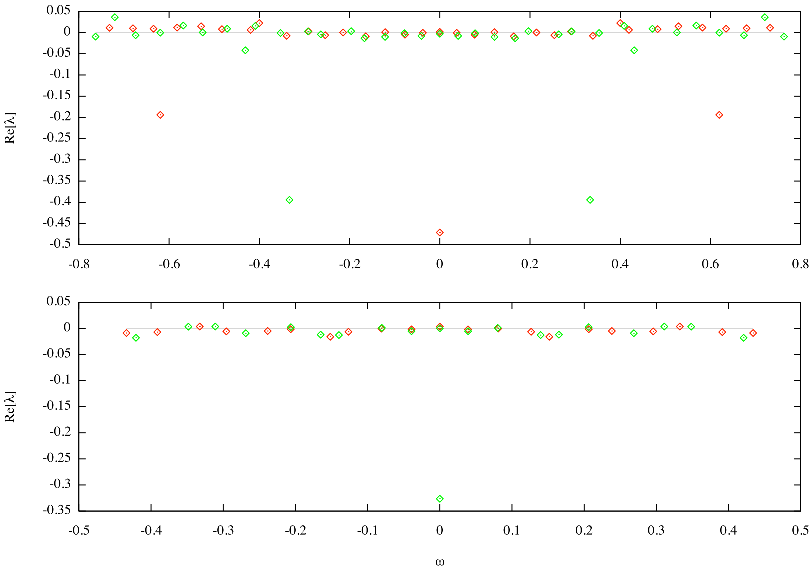

Figure 5.14: Dynamic spectrum for the time interval of 4 yrs (top) and 7 yrs (bottom). On the y-axis the stability of the mode and on the x-axis the frequency. In red the values for the GUFM model and green the COV-OBS model.

Figures 5.16 and 5.17 show the energy ranking (norm) of each mode, in logarithmic scale because some of the values are very small and hard to see. Figure 5.16 is for the time interval of 4 yrs, for both models, with each figure showing the two energy rankings discussed before, the initial norm (red) and the final norm (green) for comparison. Figure 5.17 has the same outline but now for the time interval of 7 yrs.

One can see from these figures that the top three norms correspond to the lowest frequency modes, the ones discussed before. Some modes show a bigger initial norm than a final norm, and these are the damped modes, the ones that decay quickly with time, others show the opposite, smaller initial norm than final norm, and these correspond to the unstable modes, others don't vary much, meaning they are relatively stable.

It is important to note that these graphics (5.16 and 5.17) differ from the one in figure 4.5 mainly because only half the modes are represented, the ones with zero or greater than zero imaginary λ component.

And no graphic similar to figure 4.3 was shown for this decomposition because the information about the stability that it provides can be obtained from figure 5.14 and on top of that, figure 5.14 also provides the frequency of each mode.

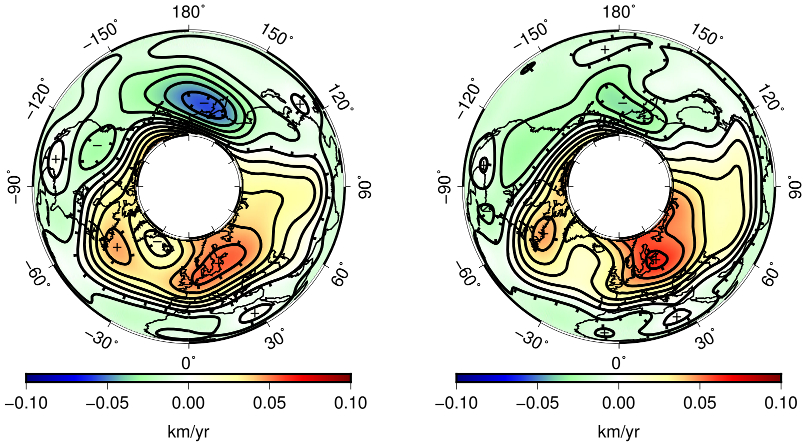

(a) T = ∞ (b) T = ∞

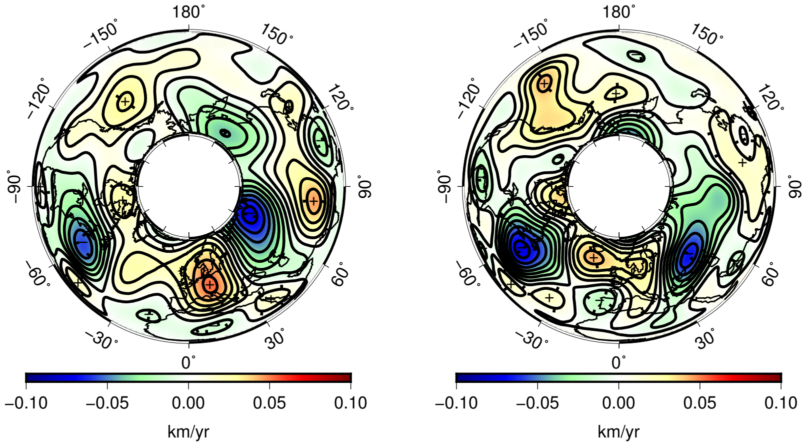

(c) T = 160.68 years (d) T = 160.43 years

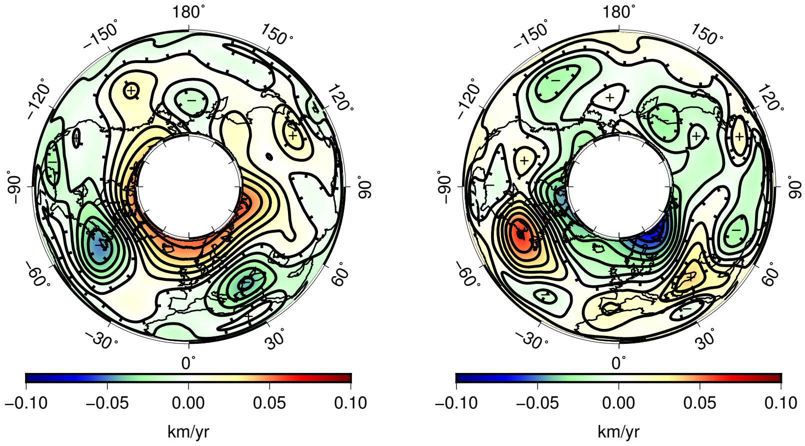

(e) T = 77.70 years (f) T = 78.32 years

Figure 5.15: Dynamic modes plotted as stream functions, in a view from the north pole, showing latitudes between 0° and 70°. GUFM model (left) and COV-OBS model (right) for a time interval of 7 yrs. Modes represented here are highlighted in tables 5.4 and 5.5, from top to bottom in the same sequence as the tables.

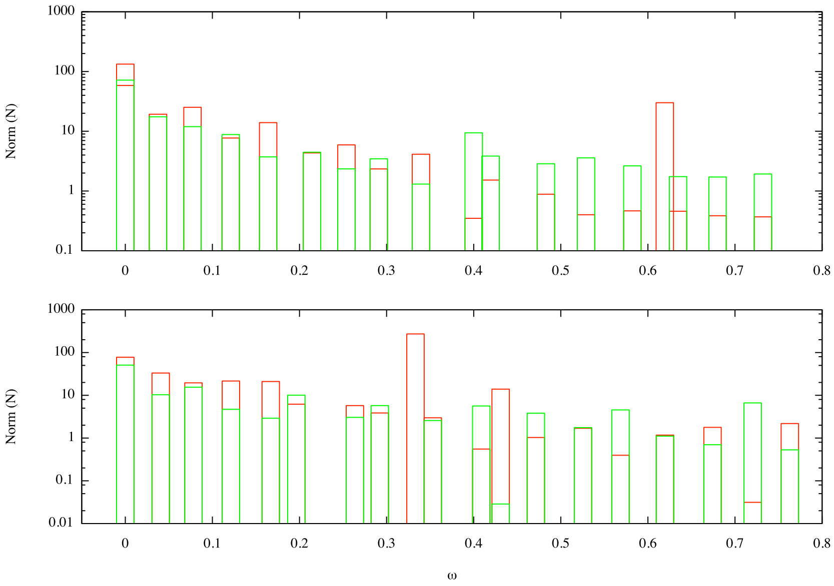

Figure 5.16: Energy ranking (logarithmic scale) according to frequency for the GUFM model (top) and COV-OBS model (bottom), for the time interval of 4 yrs. Each graphic shows both the initial energy (red) and the final energy (green) for each mode.

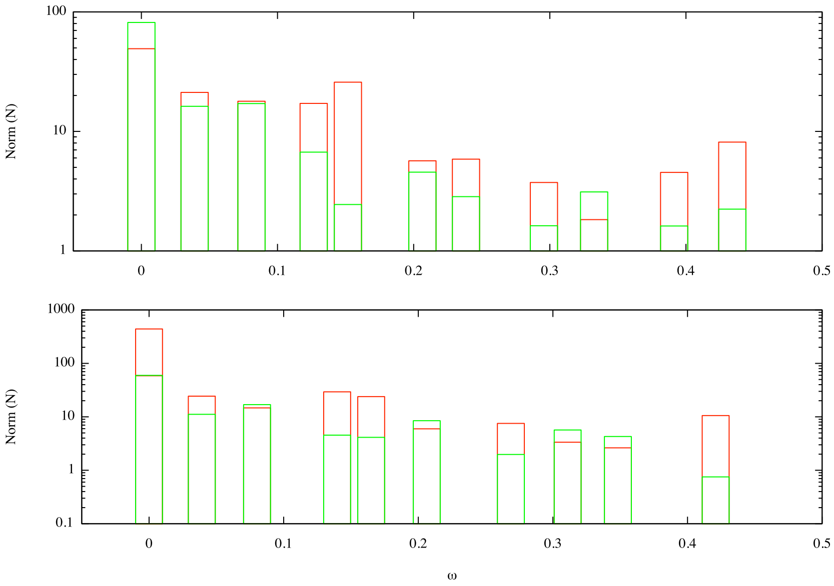

Figure 5.17: Energy ranking (logarithmic scale) according to frequency for the GUFM model (top) and COV-OBS model (bottom), for the time interval of 7 yrs. Each graphic shows both the initial energy (red) and the final energy (green) for each mode.

5.2.3 Predictions

As discussed in chapter 3, a prediction of the future behaviour of the system can be sought.

In figure 5.18 the reconstruction of the core flow can be seen. Using the flow charts from 1840 to 1990 from the COV-OBS model to create the dynamic modes, the flow was recreated for the year 1990 using the equation 3.22. As one can see, it recreates the flow inverted from the geomagnetic model exactly, as it is expected, since the snapshot for the year 1990 is included in the construction of the dynamic modes. The residual norm for the recreated flows (rec) is almost always 0, with only 3 cases, in the 10 studied not being zero. The residual norm for the recreated flows in those cases was between 1.4×10^{-12} and 2.5×10^{-11}.

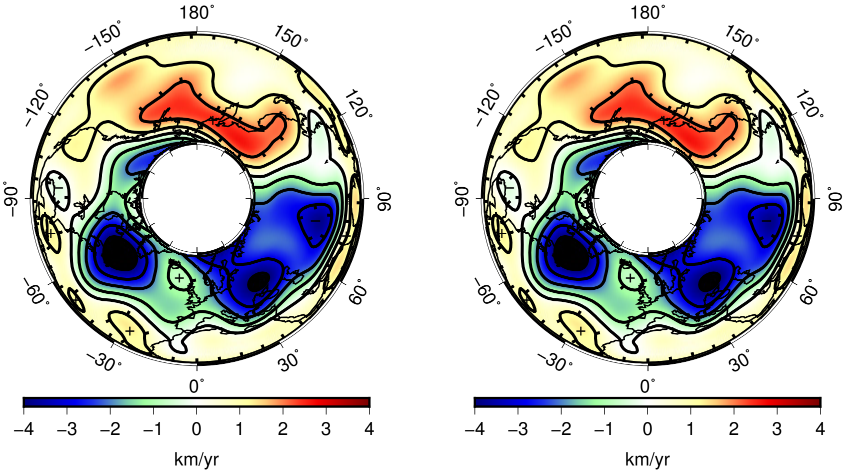

(a) COV-OBS 1990 (b) Recreation 1990

Figure 5.18: Flow obtained by the COV-OBS model (obs) for the year 1990 (left) and recreation (rec) of the flow using the method described in 3.22 with a time interval of 5 yrs (right).

By not using all the snapshots available for the construction of the dynamic modes, predictions can be made and compared to the actual snapshots for the years that were not used. The COV-OBS model was used for this purpose, since for that model the snapshots go further until the year 2010, and only the time period of 1840-1990 was used to generate the dynamic modes. The flow charts for the years 1990 to 2010 can then be used to compare with the predictions made from the dynamic modes.

In the following we distinguish between the flow chart directly inverted from geomagnetic field models and which we call 'observed' (obs); the flow chart 'recreated' from all the DMD modes (rec) for an epoch lying inside the analysed period; the flow chart 'predicted' from DMD modes for an epoch lying outside the time interval used to compute those modes (pre).

In figure 5.19 the residual norm (r) or prediction error is shown, it is obtained by the norm of the difference between the prediction and the actual flow chart (observed) divided by the norm of the actual flow chart (see equation 5.1).

$$r_k = \frac{|v_k^{obs} - v_k^{pre}|}{|v_k^{obs}|} \tag{5.1}$$

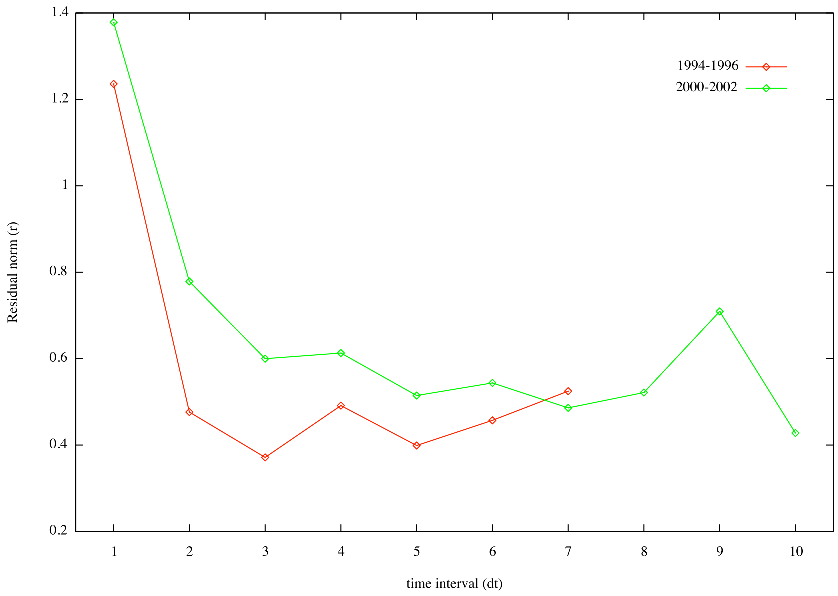

Figure 5.19: Residual norm for the predictions of the years 1994-1996 (red) and 2000-2002 (green) for time intervals ranging from 1 to 10 yrs.

It was calculated using intervals between two consecutive snapshots (dt) of 1 yr to 10 yrs , and concentrating on the ability of the method to predict the flows in the two periods, 1994-1996 and 2000-2002. We could not test the prediction capacity for one exact epoch, due to the nature of the equation used to predict the flows (equation 3.22). It only allows us to make predictions for years spaced by the time interval chosen, that is to say, starting from 1840 only multiples of the time interval are allowed. For example, in the case of the interval of 4 yrs, the last snapshot used for the decomposition is from the year 1988, while for the time interval of 5 yrs is the year 1990.

The period of 2000-2002 was the only one for each there was a prediction when using all time intervals, but the period of 1994-1996 is also shown even if only for the first 7 time intervals, for a more complete analysis. Despite the fact the predictions are not all for the same year, which accounts for some irregularities, most noticeably, the peak for the time interval of 9 yrs, an almost monotonous decrease of r with dt is seen for the 2000-2002 period, and a tendency for r to increase with the largest dt is seen for the 1994-1996 period.

From the information available, it is not clear if the residual norm will decrease continuously while increasing the time interval, as the green curve could suggest (figure 5.19). I expect that it will only decrease until a certain point and then start increasing, due to the reduced data used to calculate the dynamic modes.

From figure 5.19, for the period of 1994-1996 it seems that a time interval of 3 yrs and 5 yrs gives the best results, while for the period of 2000-2002, the intervals of 5, 7 and 10 yrs seem to give lower residual norms. In figure 5.20 results for all the time intervals from 1 to 10 yrs are shown in greater detail, for the whole epoch available for comparison (1990-2010). For a given dt, the further into the future the flows are calculated, the greater the residual norm, which means the predictions are progressively worse.

The time interval $dt = 5$ yrs was used to show the recreated (rec) (figure 5.18) and the predicted (pre) (figure 5.21) flows. For the prediction using this time interval, four years are possible, 1995, 2000, 2005 and 2010, and the first three are shown here (see figure 5.21).

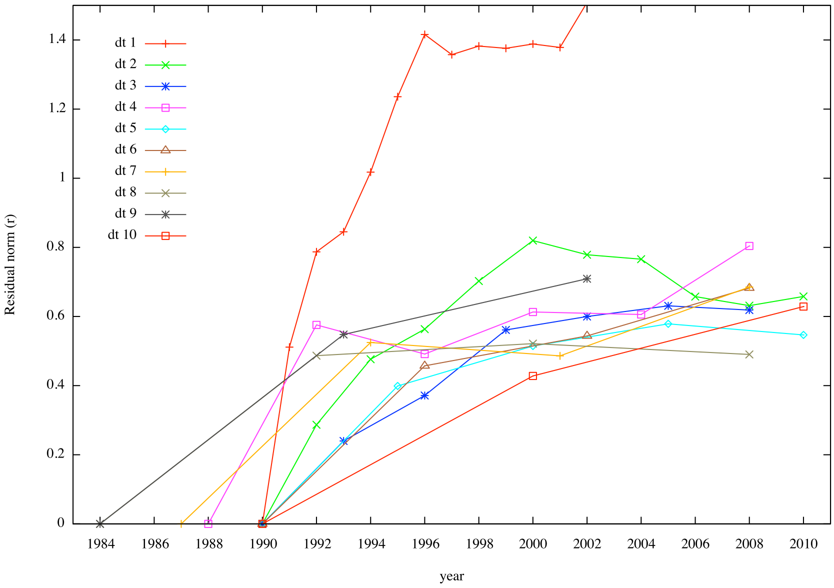

Figure 5.20: Residual norm for the time intervals between 1 and 10 yrs, for the time period of 1990-2010.

Note that not all curves in figure 5.20 start in 1990 and end in 2010, that is due to the time interval chosen, not all years can be studied for all time intervals, as previously said. For example, in the case of the time interval of 7 yrs, by starting the decomposition in the year 1840, the last one (within the period 1840-1990) that will be used is 1987, therefore, the first prediction will be for the year 1994, and the last before 2010 will be 2008. Also, the full behaviour of the $dt = 1$ yr predictions is not shown. It escalates very rapidly and would reduce the visibility of the other curves, and having such a high residual norm value, the $dt = 1$ yr decomposition is not of interest for the prediction calculations.

The first prediction in figure 5.21 is of the year 1995, and one can see that despite it not being exactly the same as the recreation from figure 5.18, it is still very close. Some of the structures are the same, the vortex in the pacific area has the same shape, even if less intense, the opposing vortex in longitude $-60°$ is also represented and the structure around longitude $60°$ is also similar. The second prediction is for the year 2000, it shows less similarity with the actual flow, the structures at longitude $60°$ are less identifiable, the vortex seen in longitude $-60°$ is not seen in the prediction as clearly, together with the structure in the pacific area. The last image is for the year 2005, and the prediction is even more distant from the actual flow. Again, some structures are similar but overall, the flow is not the same. There was another prediction that could have been shown here, for the year 2010, but the conclusions one can take would have been the same. The further into the future one tries to predict, the greatest the error. In this case ($dt = 5$ yrs), for the year 1995, the prediction seems reasonable, but after that, even using the recreation, or the actual flow for the year 1990 would provide a better representation of the flow.

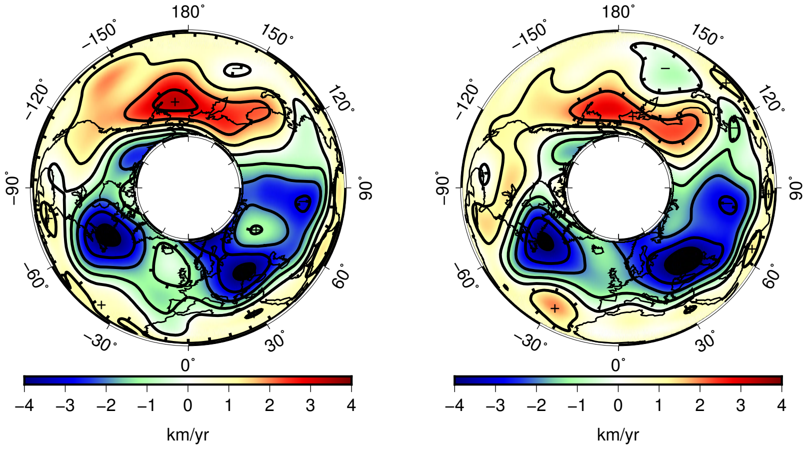

(a) COV-OBS 1995 (b) Prediction 1995

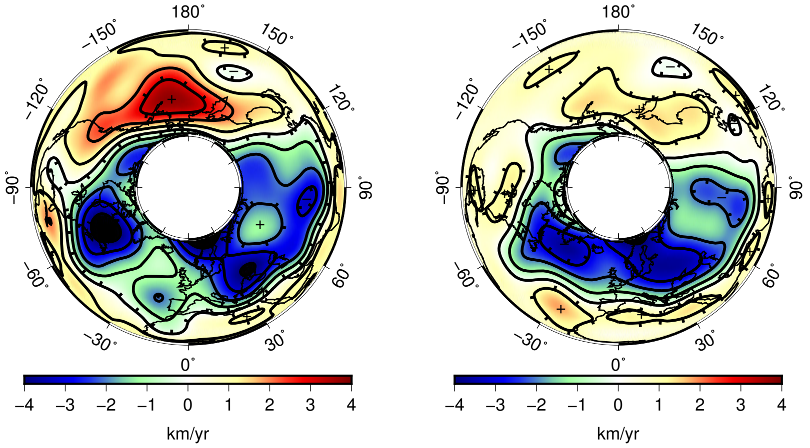

(c) COV-OBS 2000 (d) Prediction 2000

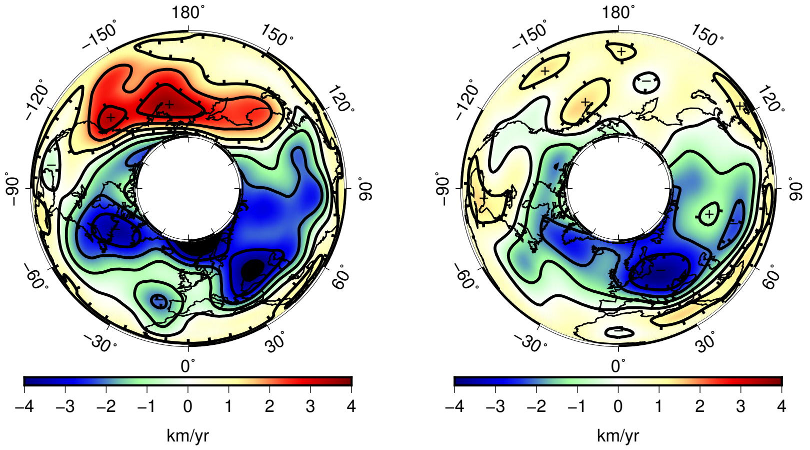

(e) COV-OBS 2005 (f) Prediction 2005

Figure 5.21: Flows obtained from the COV-OBS model dynamic modes (1840-1990) for the years of 1995 (top-left), 2000 (center-left) and 2005 (bottom-left), and the respective reconstructions using the method described in 3.22 on the right.

Chapter 6

Discussion and Conclusions

In this chapter I will summarise what was learnt during the thesis work and what could be improved and done in the future.

The case in study, the Earth's outer core flow has some dynamics that are not yet fully understood, so with this study I can only hope to provide another view on the problem and not solve it. To associate the dynamic modes that were obtained to actual physical modes, which would be the ideal ending to this study, would require the system to be well described by physical dynamical equations. A relevant question to ask is how to obtain these equations from a knowledge of the dynamical matrix A. There are many attempts made at modelling the flow in the outer core, with some very interesting results, but this identification of the modes with physical systems was not possible in my time-frame.

Nonetheless I was able to apply the DMD method to the flow charts of two systems with success, producing dynamic modes that can be visually identified with components of those flows. In particular, the well-known system of the flow inside a cavity and the case of the Earth's core flow. With respect to this latter case, three modes were discussed, among many others that were obtained. Validation of these modes was possible by comparison with results from other method (PCA) and additional dynamical information was obtained about them, that had not yet been known, as decaying time values or stability assessment and periodicities.

The Earth's geomagnetic field shows a very distinct westward drift [7], [6], most predominant in the Atlantic hemisphere, and not so visible in the Pacific. If maps of the magnetic field for different epochs are considered, a clear westward shift of structures can be identified. It is not homogenous around the globe, but it is still a very large component of the so called secular variation, which is the time variation of the magnetic field along the years.

The mean mode that was obtained, shown at the top of figures 5.12 and 5.15, has a vortex at medium latitudes in the atlantic hemisphere, loosely centred around longitude 30°, among other relevant structures. Much less intense structures exist on the opposite side, meaning it could be related to this westward drift that has been observed for many centuries now. Simulations of the Earth's core flow, considering magnetic coupling between the core and the mantle, together with an heterogeneous thermal convection from the inner core to the mantle based on an asymmetric cooling of the inner core generate flows that show similar aspects to the mean mode obtained here [2].

The second mode shown in figures 5.12 and 5.15, shows many vortices around the tangent cylinder, some more defined than others. From the quasi-geostrophic approximation (see appendix A) used for the derivation of the flows, this mode represents the structuring of the flow into cylinders parallel to the rotation axis. As said before the period associated to this mode sorting from DMD may not be relevant due to the fact that it coincides with our total time interval, but it can also mean that it represents a different component of the mean mode.

The last mode shown in figures 5.12 and 5.15 shows a large scale vortex around the tangent cylinder, together with some other smaller scale vortices around the tangent cylinder. By analysing the results and conclusions in [15], one can see that this mode carries most of the angular momentum of the flow. This is an important point because of its implications with the length of day (LOD) variation. The length of day is not constant as one might expect, it has small variations along the years, and even though they are in the range of milliseconds, they are still meaningful.

The core-mantle system can be considered isolated in the time-frames considered and so the total angular momentum variation is zero. Therefore the angular momentum variation seen in the core is the opposite of the one seen in the mantle, and the LOD variations are considered to have a source in the variation of the angular momentum of the core. This closely connects our dynamic mode with the LOD variations.

A first attempt at using the dynamic modes to predict the future of the system was made. If more information about the dynamics behind each mode was known, allowing for a selection of the relevant modes from the less relevant and many times more complex modes, better predictions could have been made.

If there was more time, the criteria for the selection of the most important modes would have been the next step, allowing to recreate the system without allowing for turbulent behaviours to distort our predictions. In other words, which modes should be kept and which could be rejected in order to reduce the flow complexity keeping the main relevant features?

The SWARM mission, composed of three satelites with sophisticated magnetometers and launched into orbit late 2013, is providing the most accurate and recent information about the geomagnetic field and its time variations. It would be very interesting to apply this method to the new models provided by the mission, particularly to study the predictive capacity of DMD. This is important to identify important space weather events: if the internal magnetic field is weakened, more space weather events are to be expected, for example due to increased solar activity, and the ability to predict those events would be an invaluable tool.

References

[1] George B. Arfken and Hans J. Weber. *Mathematical Methods for Physicists*. Academic Press, sixth edition, 2005. 42

[2] Julien Aubert, Christopher C. Finlay, and Alexandre Fournier. Bottom-up control of geomagnetic secular variation by earth's inner core. *Nature*, 502(12574):219–223, October 2013. 38, 56

[3] Ulrich R. Christensen. Geodynamo models: Tools for understanding properties of earth's magnetic field. *Physics of the Earth and Planetary Interiors*, 187:157–169, 2011. xiii, 1, 7, 36

[4] OpenFOAM Foundation. Fluid dynamics program openfoam. http://www.openfoam.com/, July 2014. 2, 17

[5] N. Gillet, D. Jault, C. C. Finlay, and N. Olsen. Stochastic modeling of the earth's magnetic field: Inversion for covariances over the observatory era. *Geochemistry Geophysics Geosystems*, 14(4):766–786, 2013. 8

[6] R. Holme. Large-scale flow in the core. In *Treatise on geophysics*, pages 107–130. Elsevier, 2007. 56

[7] A. Jackson and C. C. Finlay. Geomagnetic secular variation and its applications to the core. In *Treatise on geophysics*, pages 147–193. Elsevier, 2007. 56

[8] Andrew Jackson, Art R. T. Jonkers, and Matthew R. Walker. Four centuries of geomagnetic secular variation from historical records. *Philosophical Transactions of the Royal Society of London A*, 358:957–990, 2000. 8

[9] L. P. Jackson and J. E. Mound. Geomagnetic variation on decadal time scales: What can we learn from empirical mode decomposition? *Geophysical Research Letters*, 37, 2010. 39

[10] M. R. Jovanović, P. J. Schmid, and J. W. Nichols. Low-rank and sparse dynamic mode decomposition. Annual research briefs, Center for Turbulence Research, 2012. 20, 43

[11] Kevin k. Chen, Jonathan H. Tu, and Clarence W. Rowley. Variants of dynamic mode decomposition: boundary condition, koopman, and fourier analyses. *Journal of Nonlinear Science*, 22(6):887–915, 2012. 2

[12] Maureen Long. Using principal component analysis and dynamic mode decomposition to analyze spatio-temporal data. Master's thesis, University of California, Merced, 2011. 15

[13] Nils Olsen, Gauthier Hulot, and Terence J. Sabaka. Sources of the geomagnetic field and the modern data that enable their investigation. In *Hanbook of Geomathematics*, pages 105–124. Springer-Verlag Berlin Heidelberg, 2010. xiii, 1, 2, 3, 7

[14] M. A. Pais and D. Jault. Quasi-geostrophic flows responsible for the secular variation of the earth's magnetic field. *Geophysical Journal International*, 173:421–443, 2008. 1

[15] M. A. Pais, A. L. Morozova, and N. Schaeffer. Variability modes in core flows inverted from geomagnetic field models. Submitted to Geophys. J. Int., 2014. 32, 37, 38, 56, 65

[16] M. A. Pais, O. Oliveira, and F. Nogueira. Nonuniqueness of inverted core-mantle boundary flows and deviations from tangential geostrophy. *Journal of Geophysical Research*, 109, 2004. 2

[17] Clarence W. Rowley, Igor Mezić, Shervin Bagheri, Philipp Schlatter, and Dan S. Henningson. Spectral analysis of nonlinear flows. *Journal of Fluid Mechanics*, 2009. 14

[18] P. J. Schmid, L. Li, M. P. Juniper, and O. Pust. Applications of the dynamic mode decomposition. *Theoretical and Computational Fluid Dynamics*, 25:249–259, 2011. 15

[19] Peter J. Schmid. Dynamic mode decomposition of numerical and experimental data. *Journal of Fluid Mechanics*, 656:5–28, 2010. 2, 9, 14, 17

[20] Abu Seena and Hyung Jin Sung. Dynamic mode decomposition of turbulent cavity flows for self-sustained oscillations. *International Journal of Heat and Fluid Flow*, pages 1098–1110, 2011. 17

Appendix A

Quasi-geostrophic approximation and pseudo-stream function

To analyse the constraints that the quasi-geostrophic approximation imposes, one first must look at the governing equation, in this case the conservation of momentum for an electrically-conducting, rotating and incompressible fluid ($\nabla \cdot \vec{u} = 0$).

$$\rho \frac{\partial \vec{u}}{\partial t} + \rho(\vec{u} \cdot \nabla)\vec{u} + 2\rho(\vec{\Omega} \times \vec{u}) = -\nabla p + \vec{j} \times \vec{B} + \rho' \vec{g} + \rho \nu \nabla^2 \vec{u} \tag{A.1}$$

Where ρ is the hydrostatic density, $\vec{u}$ is the fluid velocity, $\vec{\Omega}$ ($\vec{\Omega} = \Omega \hat{z}$) is the Earth's rotation vector, p is the non-hydrostatic part of the pressure, $\vec{j}$ is the current density, $\vec{B}$ is the magnetic field, ρ' is the departure from the hydrostatic density (ρ), $\vec{g}$ is the gravitational acceleration and ν is the kinematic viscosity.

The restriction made by the quasi-geostrophic approximation has effect in the entire outer core volume, and is done considering that only the Coriolis and pressure forces contribute to the flow (i.e., that all other terms are lower orders of magnitude) (see equation A.2).

$$2\Omega\rho\hat{z} \times \vec{u} = -\nabla p \tag{A.2}$$

From equation A.2 we can deduce the Taylor-Proudman theorem (see equation A.3) by considering an incompressible flow and by calculating the curl of equation A.2. The Taylor-Proudman theorem shows that the flow is invariant in the direction parallel to the rotation axis, which is what gives the flow its columnar aspect.

$$\frac{\partial \vec{u}}{\partial z} = 0 \tag{A.3}$$

Noting that $\hat{z} \times \vec{u} = \hat{z} \times \vec{u_E}$, where $\vec{u_E}$ is the equatorial flow, one can write:

$$\begin{aligned} 2\Omega\rho(\hat{z} \times \vec{u_E}) \times \hat{z} &= -\nabla p \times \hat{z} \\ 2\Omega\rho\vec{u_E} &= -\nabla \times (p\hat{z}) \\ \vec{u_E} &= \nabla \times \left(\frac{-p}{2\Omega\rho}\hat{z}\right) \end{aligned} \tag{A.4}$$

The constraints in equation A.2 are only to the equatorial flow, and from equation A.4 we can see that $\nabla \cdot \vec{u_E} = 0$, so to maintain an incompressible flow ($\nabla \cdot \vec{u} = 0$) and also verify equation A.3, $\partial u_z/\partial z = 0$.

The quasi-geostrophic approximation verifies equation A.3 for all the equatorial flows, but it also has to take into account the spherical boundaries of the core, which means that $\partial u_z/\partial z$ cannot be zero.

In this case the flow can be described by equation A.5,

$$\vec{u} = \nabla \times \psi(s,\phi,t)\hat{z} + u_z(s,\phi,z,t)\hat{z} \tag{A.5}$$

with,

$$u_z(s,\phi,z,t) = -\frac{sz}{H_c^2}u_s(s,\phi,t) = -\frac{z}{H_c^2}\frac{\partial\psi}{\partial\phi}(s,\phi,t) \tag{A.6}$$

where (s, ϕ, z) are cylindrical coordinates, ψ is the stream function and $H_c = \sqrt{r_c^2 - s^2}$, with r_c the Earth's core radius.

The first term on the right-hand-side of equation A.5 represents the non-divergent motion, and the second term is the axial flow, needed to satisfy the non-penetrating boundary condition.

In this scheme, the Taylor-Proudman theorem (A.3) and the flow's incompressibility are not completely verified, only approximately.

A modified QG model accounts for the mass violation induced by the axial flow term in equation A.5, by adding a new term that cancels the u_z divergence (see equation A.7).

$$\vec{u} = \nabla \times \xi(s, \phi, t)\hat{z} + u_z(s, \phi, z, t)\hat{z} + \frac{s}{H_c^2}\xi\hat{\phi} \tag{A.7}$$

Where ξ is called a pseudo-stream function.

In this work, most of the representations of the flow were done using the pseudo-stream function (ξ) (referred in the work above only as stream function), but the vector ($\vec{u}$) representation of the flow was also shown, and based on the notes made in [15], one can be obtained from the other as in equation A.8.

$$\vec{u} = \frac{1}{\cos\theta}\nabla_H \wedge \xi(\theta, \phi)\hat{r} + \frac{\sin\theta}{r_c \cos^2\theta}\xi^{NZ}(\theta, \phi)\hat{\phi} \tag{A.8}$$

where $\vec{u}$ is the surface flow beneath the core-mantle boundary, ξ^{NZ} is the non-zonal part of ξ, ∇_H denotes the horizontal part of the divergence operator and (r, θ, ϕ) are the spherical coordinates.

Appendix B

Algorithm

```
%--------------------------------------------------------------------------------%
%                                                                                %
%      Dynamic Mode Decomposition Code                      Joao Domingos        %
%                                                                                %
%           -Applied to geomagnetic data         Last change:  02/09/2014        %
%                                                                                %
%--------------------------------------------------------------------------------%

%---LOAD_SNAPSHOTS-----------------------------%
Vsf = load ("Vstr.dat");   %load file with snapshots 'Vstr.dat'
cols = columns(Vsf);       %number of snapshots
%---------------------------------------------%

%---INPUT--------------------------------------%
disp("\n|------------------------------------------------------|")
disp(  "|                                                      |")
disp(  "|           |\\       |\\/|    |\\                        |")
disp(  "|           |/ynamic |  |ode |/ecomposition            |")
disp(  "|                                                      |")
disp(  "|------------------------------------------------------|")
text1 = sprintf(" Use how many snapshots? (available - %3.3d) ",cols);
numsnap = input(text1);
dt = input(" Time step:    ");
text2 = sprintf(" Calculate POD modes and projections?      ");
pod_projection = input(text2);
predict = 0;
text3 = sprintf(" Predict future behaviour? (0-No, 1-Yes)   ");
predict = input(text3);
if(predict == 1)
   text4 = sprintf(" How many %2.2d year steps into the future?   ",dt);
   future = input(text4);
end
```

```
directory = input(" Directory where the files will be stored: ","s");
disp("|----------------------------------------------------|")
%--------------------------------------------%

%---MATRIX_CALCULATIONS----------------------%
V1 = Vsf(:,1:numsnap-1);        %create the matrix V1
V2 = Vsf(:,2:numsnap);          %create the matrix V2
[U,S,W] = svd (V1);             %Single value decomposition of V1

rows = rows(Vsf);               %points in the mesh

hU = U';                        %Hermitian of U
iS = pinv(S);                   %pseudoinverse of S

FS = hU * V2 * W * iS;          %create the matrix FS

[eig_vec,eig_val] = eig(FS);    %get the eingenvalues and vectors of FS

L = diag(eig_val);              %vector with the eigenvalues
dmd = U*eig_vec;                %create the dynamic modes matrix
%--------------------------------------------%

%---OPEN_DATA_FILES--------------------------%
mkdir(directory);                  %make directory
cd(directory)                      %save into directory

fidl1 = fopen("lambda_1.dat","w");  %file with lambda_1 data
fidl2 = fopen("lambda_2.dat","w");  %file with lambda_2 data
fidf1 = fopen("files.dat","w");     %file with figure data
%--------------------------------------------%

e_proj = inv(dmd)*Vsf(:,1);

%---LAMBDA_MATRICES--------------------------%
k1 = 0;
k2 = 0;

for i = 1:rows                 %creates a matrix with non-zero eigenvalues
   if ((real(L(i)) ~= 0.0)&&(imag(L(i)) > 0.0))||\
      ((real(L(i)) >  0.0)&&(imag(L(i)) == 0.0))

      k1 += 1;
      lambda_1(k1,1) = i;                %row of the eigenvalue
      lambda_1(k1,2) = real(L(i));       %eigenvalue real part
      lambda_1(k1,3) = imag(L(i));       %eigenvalue imaginary part
      lambda_1(k1,4) = real(log(L(i))/dt);  %dynamic spectrum values real part
      lambda_1(k1,5) = imag(log(L(i))/dt);  %dynamic spectrum values imaginary part
      lambda_1(k1,6) = norm(e_proj(i)*dmd(:,i));  %energy of mode k
      if (lambda_1(k1,5) ~= 0.0)            %period of the dynamic mode k
         lambda_1(k1,7) = (2.0*pi)/(lambda_1(k1,5));
```

```
      else
         lambda_1(k1,7) = 0.0;
      end
      lambda_1(k1,8) = norm(e_proj(i)*dmd(:,i)*L(i)^(cols-1));
   end

   if (real(L(i)) >  0.0)||(imag(L(i)) ~= 0.0)

      k2 += 1;
      lambda_2(k2,1) = i;                %row of the eigenvalue
      lambda_2(k2,2) = real(L(i));       %eigenvalue real part
      lambda_2(k2,3) = imag(L(i));       %eigenvalue imaginary part
      lambda_2(k2,4) = real(log(L(i))/dt);  %dynamic spectrum values real part
      lambda_2(k2,5) = imag(log(L(i))/dt);  %dynamic spectrum values imaginary part
      lambda_2(k2,6) = norm(e_proj(i)*dmd(:,i));  %energy of mode k
      if (lambda_2(k2,5) ~= 0.0)            %period of the dynamic mode k
         lambda_2(k2,7) = (2.0*pi)/(lambda_2(k2,5));
      else
         lambda_2(k2,7) = 0.0;
      end
      lambda_2(k1,8) = norm(e_proj(i)*dmd(:,i)*L(i)^(cols-1));

   end
end
%----------------------------------------------%

%---ORDER_MODES--------------------------------%
[ss,ii] = sort (lambda_1(:,8));  %re-order de modes by their energy levels
lambda_1 = lambda_1(ii,:);
[ss,ii] = sort (lambda_2(:,8));
lambda_2 = lambda_2(ii,:);
%----------------------------------------------%

%---SCREEN_PRINT-------------------------------%
line1="|  file |  frequency |      period |     energy |      |";
line2="|------------------------------------------------------|";
disp(line1)
disp(line2)
fputs(fidf1,line1);
fputs(fidf1,"\n");
fputs(fidf1,line2);
fputs(fidf1,"\n");
%----------------------------------------------%

%---DYNAMIC_MODES------------------------------%
fini = k1;                      %final position of non-zero eigenvalues
point = 0;
for i = fini:-1:1
   point += 1;
   j = lambda_1(i,1);           %position of non-zero eigenvalue mode in dmd
```

```
   if(lambda_1(i,4) > 0)        %marks mode as stable or unstable
      stability = '(-)';
   elseif(lambda_1(i,4) <= 0)
      stability = '(+)';
   end

   frase = sprintf("   %4.4d |  %9f |  %10f |  %9f | %4s", point,lambda_1(i,5)\
,norm(lambda_1(i,7)),lambda_1(i,6),stability);
   disp(frase)
   fputs(fidf1,frase);
   fputs(fidf1,"\n");

   D(:,point) = real(dmd(:,j));  %adds dynamic mode to matrix D

   file_name1 = sprintf("dmd_%s_%4.4i.txt",directory,point);

   dmd_sf = D(:,point);

   save(file_name1,"dmd_sf","-ascii")
end
%----------------------------------------------%

%---RE-CREATE_MODES---------------------------%
if (predict == 1)
   for k = 1:future
      mode_fut = 0;
      for i = 1:rows
         mode_e(:,i) = e_proj(i)*dmd(:,i)*eig_val(i,i)^(k+cols-1);
         mode_fut = mode_fut .+ real(mode_e(:,i));
      end
      file_name2 = sprintf("pre_%s_%2.2i.txt",directory,k);
      save(file_name2,"mode_fut","-ascii")
   end
end
%----------------------------------------------%

%---POD_MODES_&_PROJECTION--------------------%
if(pod_projection == 1)
   for i = 1:rows
      V1n(i,:) = detrend(V1(i,:),0);
   end
   [U2,S2,W2] = svd (V1n);
   POD = U2;                  %POD modes
   projec = POD'*D;           %projection matrix
   hprojec = projec';         %inverse of projection matrix

   for j = 1:fini
      file_name2 = sprintf("pod_%s_%4.4i.txt",directory,j);
      pod_sf = POD(:,j);
```

```
      save(file_name2,"pod_sf","-ascii")
   end
end
%--------------------------------------------%

%---SCREEN_PRINT-----------------------------%
disp("|-----------------------------------------------------|")
disp("  period == 0.0 corresponds to infinity!")
disp("|-----------------------------------------------------|")
disp(" (+) - stable , (-) - unstable")
disp("|-----------------------------------------------------|")
disp(" DMD modes saved as: dmd_$directory_$file.txt")
if(pod_projection == 1)
   disp(" POD modes saved as: pod_$directory_$file.txt")
end
if(predict == 1)
   disp(" Predictions saved as:  pre_$directory_$i.txt")
end
disp("|-----------------------------------------------------|")
%--------------------------------------------%

%---EIGENVALUES------------------------------%
ur = lambda_2(:,2);                %real eigenvalue
ui = lambda_2(:,3);                %imaginary eigenvalue
figure(2001,"visible","off")
plot(ur,ui,".dk")                  %plots eigenvalues, real vs imaginary

frase = sprintf(" eigenvalues saved as:              eigen.png");
disp(frase)

file = sprintf("eigen.png");
print(file)
%--------------------------------------------%

%---DYNAMIC_SPECTRUM-------------------------%
lr = lambda_2(:,4);                %real value of lambda
li = lambda_2(:,5);                %imaginary value of lambda
figure(2002,"visible","off")
plot (li,lr,".dk")                 %plots dynamic spectrum

frase = sprintf(" dynamic modes spectrum saved as:   spectrum.png");
disp(frase)

file = sprintf("spectrum.png");
print(file)
%--------------------------------------------%

%---ENERGY-----------------------------------%
[ss,ii] = sort (lambda_1(:,5));    %order lambda values acording to frequency
```

```
fr = lambda_1(ii,5);               %frequency of mode
en = lambda_1(ii,8);               %energy of mode
figure(2003,"visible","off")
bar(fr,en)                         %plots energy ranking of each mode

frase = sprintf(" energy ranking saved as:           energy.png");
disp(frase)

file = sprintf("energy.png");
print(file)
%----------------------------------------------%

%---SAVE_DATA----------------------------------%
disp("|------------------------------------------------------|")
save modes.dat D %saves dynamic modes into file dmd.dat
disp(" dynamic modes saved to:            modes.dat")
lambda_topline = sprintf(" %6s %14s %14s %14s %14s %14s %14s %14s \n\n"\
                ,"#i","eig_real","eig_imag","spec_real","spec_imag","energy"\
                ,"period", "last_energy");
fputs(fidl1,lambda_topline);
fputs(fidl2,lambda_topline);

for i = 1:k1
lambda_line = sprintf(" %6i %14f %14f %14f %14f %14f %14f %14f "\
                ,lambda_1(i,1),lambda_1(i,2),lambda_1(i,3),lambda_1(i,4),\
                lambda_1(i,5),lambda_1(i,6),lambda_1(i,7),lambda_1(i,8));
fputs(fidl1,lambda_line);
fputs(fidl1,"\n");
end
disp(" short dynamic data saved to:       lambda_1.dat")

for i = 1:k2
lambda_line = sprintf(" %6i %14f %14f %14f %14f %14f %14f %14f "\
                ,lambda_2(i,1),lambda_2(i,2),lambda_2(i,3),lambda_2(i,4),\
                lambda_2(i,5),lambda_2(i,6),lambda_2(i,7),lambda_2(i,8));
fputs(fidl2,lambda_line);
fputs(fidl2,"\n");
end
disp(" complete dynamic data saved to:    lambda_2.dat")

save projection.dat hprojec -ascii
if(pod_projection == 1)
disp(" projection data saved to file:     projection.dat")
end
disp(" screen output saved to file:     files.dat")
disp("|------------------------------------------------------|")
printf(" files saved in folder:             %s\n", directory)
disp("|------------------------------------------------------|\n")
disp(asctime (localtime (time ())))
%----------------------------------------------%
```

```
%---CLOSE_DATA_FILES--------------------------%
fclose(fidl1);
fclose(fidl2);
fclose(fidf1);
close all;
%--------------------------------------------%
```